Near Neutral pH Redox Flow Battery with Low Permeability and Long-Lifetime Phosphonated Viologen Active Species

Shijian Jin, Eric M. Fell, Lucia Vina-Lopez, Yan Jing, P. Winston Michalak, Roy G. Gordon,* and Michael J. Aziz*

A highly stable phosphonate-functionalized viologen is introduced as the redox-active material in a negative potential electrolyte for aqueous redox flow batteries (ARFBs) operating at nearly neutral pH. The solubility is 1.23 M and the reduction potential is the lowest of any substituted viologen utilized in a flow battery, reaching −0.462 V versus SHE at pH = 9. The negative charges in both the oxidized and the reduced states of 1,1′-bis(3-phosphonopropyl)-[4,4′-bipyridine]-1,1′-diium dibromide (BPP–Vi) effect low permeability in cation exchange membranes and suppress a bimolecular mechanism of viologen decomposition. A flow battery pairing BPP–Vi with a ferrocyanide-based positive potential electrolyte across an inexpensive, non-fluorinated cation exchange membrane at pH = 9 exhibits an open-circuit voltage of 0.9 V and a capacity fade rate of 0.016% per day or 0.00069% per cycle. Overcharging leads to viologen decomposition, causing irreversible capacity fade. This work introduces extremely stable, extremely low-permeating and low reduction potential redox active materials into near neutral ARFBs.

1. Introduction

The cost of renewable electricity from photovoltaics and wind has decreased significantly over the last four decades to the point that these clean resources have become realistic alternatives to fossil fuels for generating electricity.[1-3] However, unlike burning fossil fuels, which is easily tunable to meet human needs, wind and solar are unpredictable and intermittent due to day/night shift and seasonal changes, which hampers their penetration into the electrical grid.[4] The incorporation of safe, low-cost and large-scale energy storage into the electrical grid could solve this problem.[2] The most well-known and most widely applied grid-scale energy storage is pumped-hydro storage,

but its specific geographical requirement forestalls universal application, and concerns over ecosystem destruction limit its growth even in accommodating geographies. Other energy storage methods such as lithium-ion batteries, compressed-air, and fuel cells share a limited portion of the energy storage market because of their high cost, safety concerns, limited discharge duration, low energy efficiency, or other difficulties.[5] Aqueous redox flow batteries, possessing non-flammable electrolytes, decoupled energy/power scaling, and potential low cost, demonstrate strong potential for grid-scale energy storage.[6] Several MW/MWh sized all-vanadium flow batteries (VRFBs) have been installed across the globe.[7,8] However, widespread deployment of VRFBs is hindered by the high and volatile price of vanadium. Organic redox-active materials, composed of earth-abundant elements such as C, H, O, N, S, and P, potentially have lower and more stable costs compared to vanadium.[9,10] Another unique benefit of organic molecules is their structural tunability, which enables various beneficial properties such as stability, solubility, proper redox potential, fast kinetics, and low toxicity to be pursued by the research community.

Quinones and viologens are among the most studied organic molecules for aqueous redox flow battery (ARFB) negolytes (negative electrolytes) because of their chemical stability and fast kinetics.[11] Ionic or nonionic groups such as $-SO_3^-$,[12,13] $-O^-$,[14-16] $-COO^-$,[17,18] $-PO_3^{2-}$,[19] $-NR_3^+$,[20] and poly-ethylene glycol[21] have been tethered to redox active cores to achieve reasonable solubilities in aqueous solutions. Quinones, though undergoing two-electron redox processes, are usually operable in extreme pH (pH = 0 or pH > = 12).[12,14,17] Recently, quinones soluble at near neutral pH (pH = 7–9) have been developed, but the electrolyte pH still swings considerably (up to pH = 13) due to proton coupled electron transfer during charging.[19,21] On the other hand, viologens are soluble at pH = 7 and their redox reactions do not involve coupled protons or hydroxides, thus maintaining stable pH during cycling. Therefore, viologen electrolytes can be less corrosive to electrolyte-contacting materials, which potentially reduces maintainance cost. Another advantage of having near neutral solution is the high stability and solubility of ferrocyanide, which is the most promising posolyte (positive electrolyte) in terms of stability.[11,17,22] First generation viologen-based flow batteries utilized methyl viologen (MV) electrolytes as active material. The high solubility of MV

S. Jin, E. M. Fell, L. Vina-Lopez, Prof. R. G. Gordon, Prof. M. J. Aziz
John A. Paulson School of Engineering and Applied Sciences
Harvard University
Cambridge, MA 02138, USA
E-mail: gordon@chemistry.harvard.edu; maziz@harvard.edu
Dr. Y. Jing, Prof. R. G. Gordon
Department of Chemistry and Chemical Biology
Harvard University
Cambridge, MA 02138, USA
P. W. Michalak
Harvard College
Cambridge, MA 02138, USA

ADVANCED
SCIENCE NEWS
www.advancedsciencenews.com

ADVANCED
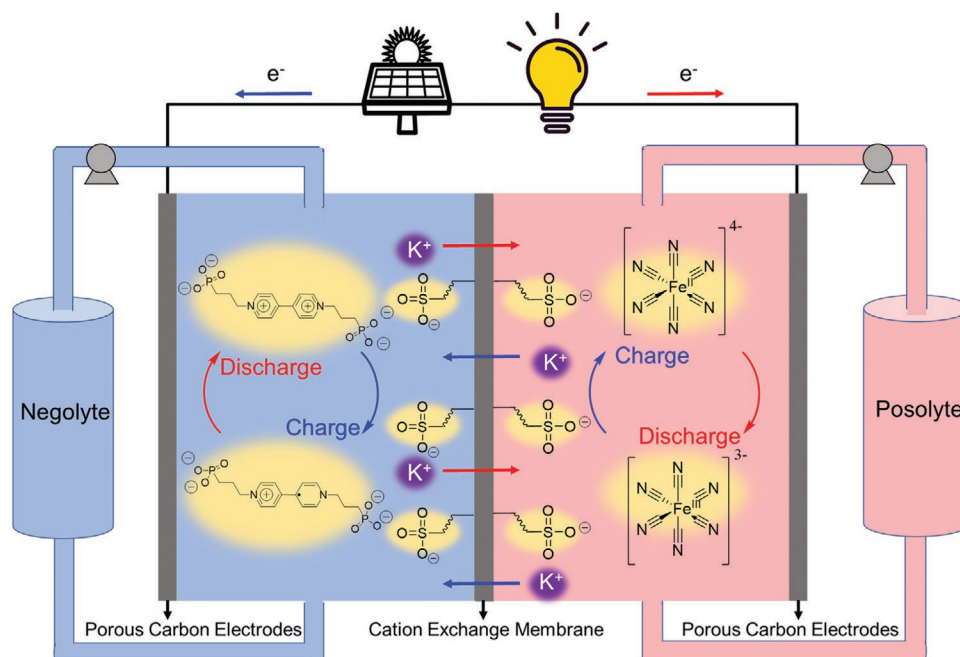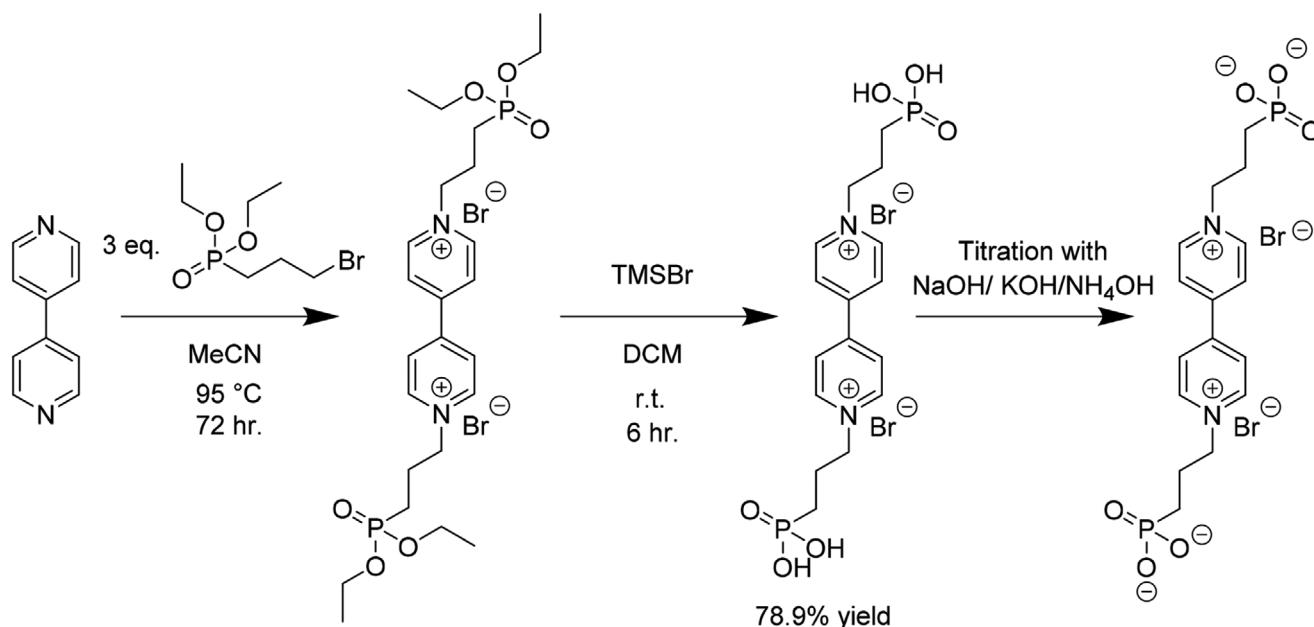ENERGY
MATERIALS
www.advenergymat.de

Figure 1. Scheme of BPP–Vi | ferrocyanide flow battery with enlarged reaction chamber. Negatively charged species are highlighted in yellow. Red arrows refer to a galvanic (discharging) process and blue arrows refer to an electrolytic (charging) process. Both the oxidized and the reduced forms of BPP–Vi are negatively charged, so they are repelled by the sulfonate-rich membrane, which minimizes BPP–Vi permeation.

in neutral pH solution and its fast kinetics, decent reduction potential (–0.45 V vs SHE, ≈0.9 V cell voltage when paired with ferrocene derivatives) and facile synthesis have been demonstrated by researchers.[18,23,24] However, MV-based flow batteries experience high capacity fade rates on the order of ≈1% per day, caused by both MV permeating through membranes and a bimolecular decomposition mechanism.[20] Beh et al. addressed both of these issues by tethering trimethyl ammonium groups to the viologen core to make a +4 charged bis(3-trimethylammonio)propyl viologen tetrachloride (BTMAP–Vi).[20] The high number of positive charges enhances the repulsion among viologen molecules as well as the repulsion between viologen and the positively charged anion exchange membrane (AEM). However, the drawback is that the presence of electron-withdrawing trimethyl ammonium groups raises the reduction potential of BTMAP–Vi to –0.36 V versus SHE, causing lower cell voltage and low power density. DeBruler et al. have demonstrated a sulfonated viologen zwitterion 1,1′-bis(3-sulfonatopropyl)-4,4′-bipyridinium ((SPr)$_2$V) that has a reduction potential of –0.43 V versus SHE and is compatible with cation exchange membranes (CEM) such as Nafion series and Selemion CSO, which have lower resistance than the AEMs used by Beh et al.[13] Pairing the (SPr)$_2$V based negolyte with (NH$_4$)$_4$Fe(CN)$_6$ or Br$^-$ in a flow cell achieved power densities of 99[25] and 227 mW cm^{-2},[26] respectively. However, because of low charge in the oxidized (0 charge) and reduced state (–1 charge), (SPr)$_2$V permeates through the CEM at a high rate.[25] Although Luo et al. addressed this issue by putting (SPr)$_2$V on both sides of the CEM to balance the chemical potential, full material utilization was sacrificed, thus raising cost and lowering specific energy, and potentially creating complicating interactions among active species.[20,25]

This work presents a phosphonate group–substituted viologen, i.e., 1,1′-bis(3-phosphonopropyl)-[4,4′-bipyridine]-1,1′-diium (**BPP–Vi**), which has a –2 charge in the oxidized state and –3 charge in the reduced state at pH = 9. The negative charge makes **BPP–Vi** less susceptible to bimolecular decomposition and slows permeation through a CEM (**Figure 1**), compared with previously developed viologens. Pairing **BPP–Vi** with ferrocyanide and utilizing a cheap hydrocarbon-based Fumasep E620(K) CEM, our 1 M high **BPP–Vi** concentration full cell exhibits an open-circuit voltage (OCV) of ≈0.9 V and an extremely low capacity fade rate [11] of 0.016% per day or 0.00069% per cycle. No crossover of electroative material from either posolyte or negolyte was detected after extended cycling. A power density of 143 mW cm^{-2} was achieved, which is 44% higher than that of previously demonstrated viologen|ferrocyanide cells.

2. Results and Discussion

BPP–Vi was synthesized through a simple S$_N$2 reaction, followed by a hydrolysis of the ester (**Scheme 1**). Each step was purified through simple filtration and the overall yield was 79% with high purity over the two steps (Figures S1–S2, Supporting Information). The facile synthesis and purification facilitate industrial large-scale production since neither catalyst nor resource-intensive chromatography are needed. Solubility of **BPP–Vi** was measured through UV–Vis spectrophotometry and the maximum solubility is 1.23 M (Figure S4, Supporting Information). Titration (**Figure 2**a) of the 0.1 M **BPP–Vi** solution shows that the pK_{a1} and pK_{a2} are the same as phosphonic acid, located at pH = 2 and pH = 7, respectively.

ADVANCED
SCIENCE NEWS
www.advancedsciencenews.com

ADVANCED
ENERGY
MATERIALS
www.advenergymat.de

Scheme 1. Synthesis of BPP–Vi through substitution of diethyl (3-bromopropyl)phosphonate with 4,4′-bipyridine, followed by deprotection by bromotrimethylsilane.

Reaction kinetics of **BPP–Vi** were evaluated through cyclic voltammetry (CV) at different pH (Figure S6, Supporting Information). Figure 2b shows that the reduction potentials of the first and second redox pairs of **BPP–Vi** do not vary significantly with pH, which suggests that proton coupled electron transfer does not occur. The slight variation in reduction potential is caused by different buffer compositions and different degrees of phosphonate ionization. At slightly acidic pH, both redox processes of **BPP–Vi** are irreversible, signified by the small or non-existent oxidation peak (Figure S6, Supporting Information). At highly basic pH (pH = 14), the small side peak near −0.9 V versus SHE suggests that decomposition, i.e., cleavage of one of the alkyl chains, of **BPP–Vi** has occurred (Figure S6, Supporting Information). Reversible CV peaks were obtained over pH range 8.1–13.0, which aligns with the fully deprotonated region from the titration curve. At pH = 9, the reduction potential of **BPP–Vi** is −0.46 V versus

SHE (Figure 2c), which will deliver a cell voltage of 0.9 V when paired with ferrocyanide, and this pH was used in further cell tests. Linear sweep voltammetry with a rotating disk electrode of a 5×10^{-3} M **BPP–Vi** solution was performed at pH = 9 and demonstrated a diffusion coefficient of 2.7×10^{-6} cm^2 s^{-1} for the oxidized form and 2.6×10^{-6} cm^2 s^{-1} for the singly reduced form (Figure S7, Supporting Information). The rate constant for the first and second reduction reactions were determined to be 2.9×10^{-3} and 2.2×10^{-3} cm s^{-1}, respectively (Figure S8–S9, Supporting Information).

To investigate the chemical and electrochemical stability of **BPP–Vi**, thermal stability tests and symmetric cell cycling of **BPP–Vi** were conducted. 0.1 M **BPP–Vi** solutions at pH = 9 were stored at 65 °C for one week. Proton nuclear magnetic resonance (^{1}H NMR) experiments conducted at the beginning and the end of the week revealed that the oxidized form of **BPP–Vi** is stable at the elevated temperature, which infers
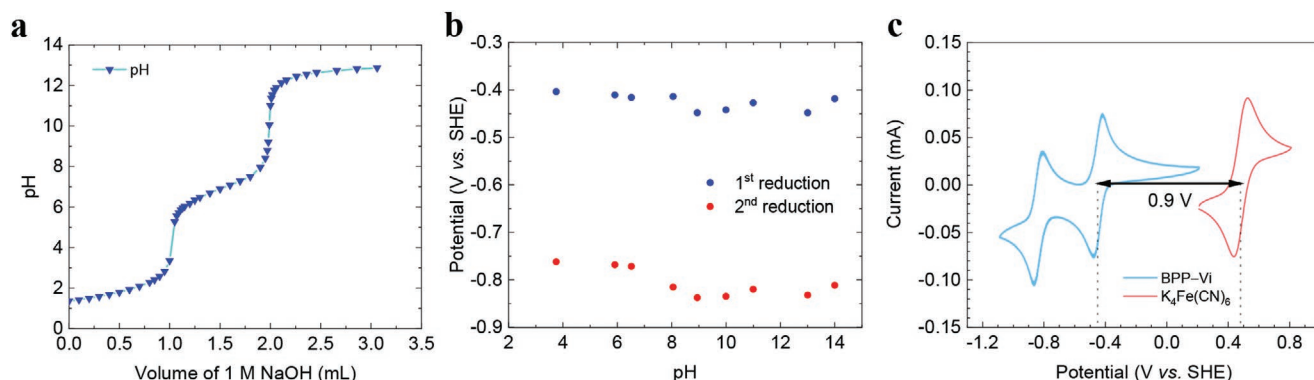

Figure 2. Characterization of BPP–Vi. a) Titration of 5 mL 0.1 M BPP–Vi with 1 M NaOH shows that the pK_{a1} of BPP–Vi is near pH = 2 and pK_{a2} is near pH = 7. b) The reduction potentials of both BPP–Vi redox reactions versus pH. The most negative reduction potential is achieved at pH = 9. c) Pairing BPP–Vi with K$_4$Fe(CN)$_6$ at pH = 9 can lead to an equilibrium potential of 0.9 V.
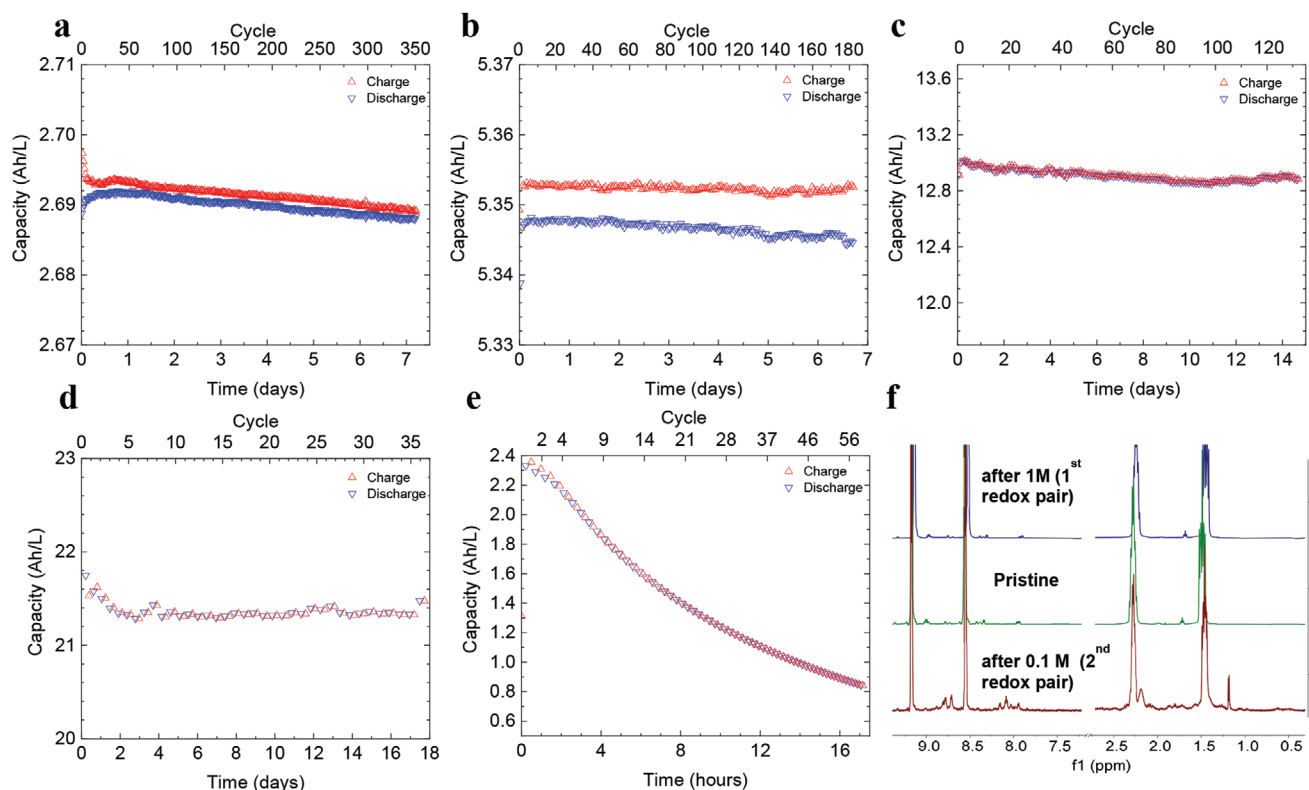
Figure 3. Volumetrically unbalanced compositionally symmetric cell cycling of BPP–Vi. The capacity limiting side has 6 mL of a) 0.1 M b) 0.2 M c) 0.5 M and d) 1 M BPP–Vi solution in 1 M KCl at pH = 9 and the non-capacity limiting side has 11 mL of the same concentration solution. Only the 1st (BPP–Vi^{2-}/BPP–Vi^{3-}) redox couple was accessed in a), b), c) and d). In e), only the 2nd (BPP–Vi^{3-}/BPP–Vi^{4-}) redox couple was accessed and the capacity decreased much more quickly. f) NMR spectra of BPP–Vi after cycling in d), pristine BPP–Vi, and BPP–Vi after e).

even higher chemical stability at lower temperature (Figure S5, Supporting Information). The stability of **BPP–Vi** in a battery was examined through potentiostatic cycling in a volumetrically unbalanced compositionally symmetric cell in a N$_2$-filled glovebox. Several works have previously shown that symmetric cell cycling is a simple and efficient way to understand the chemical and electrochemical stability of flow battery reactants, because confounding factors such as reactants crossing over the membrane are suppressed.[17,19,27] Cycling of 0.1 M **BPP–Vi** for 7 days and 350 cycles in a symmetric cell exhibited an extremely low fade rate of 0.014% per day or 0.0004% per cycle (**Figure 3**a). The cell was paused at the fully charged and fully discharged state for 4 and 2 days, respectively, and the temporal fading rate during these two periods was approximately equal to the cycling fading rate (Figure S12, Supporting Information). Symmetric cell cycling of 0.2 M **BPP–Vi** for 7 days and 0.5 M **BPP–Vi** for 16 days, exhibited fade rates of 0.0023% per day (0.0001% per cycle, Figure 3b) and 0.058% per day (0.0065% per cycle, Figure 3c), respectively; both fade rates are of the same order of magnitude as the rate at 0.1 M. For the 18-day symmetric cell cycling of 1 M **BPP–Vi**, only 80% of the theoretical capacity was accessed due to high mass transport resistance, so the fading rate is inexplicable through cycling data (Figure 3d). However, ex situ chemical analysis, such as nuclear magnetic resonance (NMR) spectroscopy and liquid chromatography–mass spectrometry (LC–MS) did not show

any evidence of decomposition products (Figures S15–S19, Supporting Information).

The extensive symmetric cell cycling results are on par with previously reported fading rates of BTMAP–Vi.[27] In that work, the decomposition of methyl viologen (MV), which could be generalized to all viologen derivatives, is attributed to the dimerization of the reduced species, MV$^{·+}$, followed by a disproportionation reaction that forms the oxidized species MV^{2+} and the doubly reduced species MV^0, which can be protonated by water irreversibly to form a redox-inactive species.[20,28] DeBruler et al. presented results where two electrons are accessed during the cycling of 0.25 M BTMAP–Vi but the fading rate is 0.9% per day (0.01% per cycle), which is 9 times and 27 times faster than the fading in the cycling of 1.3 M and 0.75–1 M BTMAP–Vi, respectively, when only the first electron is accessed.[29] Both pieces of evidence suggest that accessing the doubly reduced species, either created through disproportionation or direct reduction, leads to instability. We wanted to determine whether **BPP–Vi** suffers the same fate. We name the oxidized form, singly reduced form and doubly reduced form of **BPP–Vi** to be **BPP–Vi^{2-}**, **BPP–Vi^{3-}**, and **BPP–Vi^{4-}**, respectively. 20 mL 0.1 M **BPP–Vi** solution was charged to 50% state of charge (SOC) of the 2nd electron (50% **BPP–Vi^{3-}** and 50% **BPP–Vi^{4-}**), and then 6 mL was used as the capacity limiting side (CLS) and 11 mL was used as the non-capacity limiting side (NCLS). The capacity faded by more than 60% within 17 h of cycling from 0% SOC

Table 1. Permeability of viologens through various membranes.

Molecule	Charge in the oxidized/reduced form	Membrane	pH	Permeability [cm² s⁻¹]
MV[a]	+2/+1	Selemion DSV AEM	7	3.4×10^{-9}
BTMAP–Vi[a]	+4/+3	Selemion DSV AEM	7	6.7×10^{-10}
(SPr)$_2$V	0/–1	N212 CEM	7	8.0×10^{-9}
(SPr)$_2$V	0/–1	E620 CEM	7	5.6×10^{-11}
BPP–Vi	–2/–3	N212 CEM	7	7.0×10^{-11}
BPP–Vi	–2/–3	E620 CEM	7	1.4×10^{-12}
BPP–Vi	–2/–3	N212 CEM	9	5.6×10^{-11}
BPP–Vi	–2/–3	E620 CEM	9	2.2×10^{-13}

[a]Ref. [20].

to 100% SOC of the 2nd electron (Figure 3e). The NMR spectrum of the post-cycling solution shows primarily the original **BPP–Vi**$^{2-}$ but some new peaks appear in both the aromatic and aliphatic regions (Figure 3f). The amount of decomposition product is significant. This result suggests a combination of apparent fading, possibly caused by auto-oxidation-induced imbalancing, and chemical decomposition, took place during the symmetric cell cycling of the **BPP–Vi**$^{3-}$/**BPP–Vi**$^{4-}$ pair. The molecular structure of the decomposition product is still under study, but the evidence clearly leads to the conclusion that accessing the second electron causes irreversible decomposition of **BPP–Vi**.

Based on the CV and the titration curve, the optimal electroactivity of **BPP–Vi** is achieved at pH near 9. We also expect a lower **BPP–Vi** permeability at pH = 9 compared to pH = 7 because more **BPP–Vi** molecules are deprotonated at pH = 9, thus enhancing the repulsion between the membrane and the molecules. Debruler et al. show that a CEM can exclude (SPr)$_2$V through size-exclusion[13] but Luo et al. show that material crossover still causes significant amounts of capacity fade — 2.6% per day in a full cell.[25] Comparing the permeability of **BPP–Vi** and that of (SPr)$_2$V using Nafion 212 as the test membrane at pH = 7, we find that **BPP–Vi** permeates at 7.1×10^{-11} cm² s⁻¹, which is two orders of magnitude slower than (SPr)$_2$V, at 7.8×10^{-9} cm² s⁻¹ (Figure S11, , Supporting Information; **Table 1**). At pH = 9, the permeability of **BPP–Vi** is even lower, with a rate of 4.1×10^{-11} cm² s⁻¹ (Figure S11, Supporting Information), validating our hypothesis. We also implemented an inexpensive hydrocarbon-based membrane, Fumasep E620(K), which was proven to suppress the permeation of anthraquinones and ferro/ferricyanide very well.[17,19] The permeability of ferricyanide, the more permeating species of the pair, is 4.4×10^{-12} cm² s⁻¹ across E620(K)[17] and 4.5×10^{-9} cm² s⁻¹ across Nafion 212.[30] The permeability of **BPP–Vi** through E620(K) is 1.4×10^{-12} cm² s⁻¹ at pH = 7 and 5.4×10^{-13} cm² s⁻¹ at pH = 9, which are both slower than the permeability through Nafion 212 (Figure S11, Supporting Information) (Table 1). With the lowest permeability value (5.4×10^{-13} cm² s⁻¹), it should take 910 and 6000 years to lose 10% and 50% capacity, respectively, due to **BPP–Vi** crossover (Table S1), assuming exponential behavior.[20] Figure S13 in

the Supporting Information demonstrated that E620(K) has a higher ionic conductivity at near neutral condition compared to Nafion 212. Therefore, full cell polarization and cycling experiments were conducted with E620(K) membrane at pH = 9.

Given the high chemical and electrochemical stability and low permeability through E620(K) membrane, **BPP–Vi**, paired with K$_4$Fe(CN)$_6$, was evaluated in full cells with E620(K) being the membrane at pH = 9. A 0.1 M concentration cell was charged at 10 mA cm⁻² and polarization curves were measured at 10% SOC intervals. The open-circuit voltage (OCV) increased from 0.89 V at 10% SOC to 1.0 V at 90% SOC, and the OCV at 50% SOC was 0.94 V (**Figure 4**a). The alternating current area-specific resistance (AC-ASR) of the cell was determined via high-frequency electrochemical impedance spectroscopy (EIS) and the value was slightly above 1 Ω cm² across all SOCs (Figure 4a). The proximity of the polarization resistance curve, which shows the value of direct current area-specific resistance (DC-ASR), and the high frequency resistance curve shows that more than 60% of the resistance of the cell can be attributed to the membrane resistance (Figure 4a). A peak power density of 0.145 W cm⁻² was observed at 100% SOC and the value at 50% SOC is 0.123 W cm⁻² (Figure 4b). High coulombic efficiency was realized at all current densities, thus the loss in energy efficiency is attributed to voltage efficiency, which is expected to increase when membrane resistance is lowered (Figure 4c,d). Only 30% of the capacity can be accessed at 100 mA cm⁻² because a low voltage cutoff (1.1 V) was chosen to avoid accessing the 2nd electron (Figure 4d, see below for further details).

A flow cell with 6 mL of 0.1 M **BPP–Vi** negolyte and 20 mL of 0.1 M K$_4$Fe(CN)$_6$/0.04 M K$_3$Fe(CN)$_6$ posolyte was placed in a N$_2$-filled glovebox for an extended cycling study. The small amount of ferricyanide prevents the posolyte from becoming the capacity limiting side during discharge in case it undergoes slow reductive side reactions at high SOC; this precaution permits us to focus our attention only on the stability of the negolyte. The cell was first charged at 40 mA cm⁻² with 1.2 V cutoff during charge and 0.4 V cutoff during discharge. A 2 mA cm⁻² current cutoff to a potentiostatic hold was imposed as soon as the voltage cutoffs were reached. The capacity fade rate under such conditions was 0.2% per day or 0.00068% per cycle (Figure 4e). After 500 cycles, the charging voltage cutoff was set to 1.1 V while maintaining other conditions. The capacity fade rate became 0.019% per day or 0.00013% per cycle across 4 days and 500 cycles (Figure 4e points B to C). Once the charging voltage cutoff was set to 1.2 V again, the fade rate increased by more than one order of magnitude. The cell was then cycled with 1.1 V charging voltage cutoff for 16 days or 2300 cycles. A 0.024% per day or 0.00017% per cycle capacity fade rate was maintained (Figure 4e points F to G). We increased the voltage cutoff for charge at the end of the cycling in order to check whether the fade rate was real. The capacity difference between points A and D, and that between points E and H, are consistent with the difference between points B and C, and the difference between points F and G, respectively (Figure 4e). Such consistency demonstrates that the ≈0.02% per day fading rate is real. We suspect the higher fading rate at higher voltage cutoff is due to partial access of the second electron reduction. Theoretically, according to the Nernst equation with dilute solution assumptions, neglecting ohmic, kinetic, and mass-transport
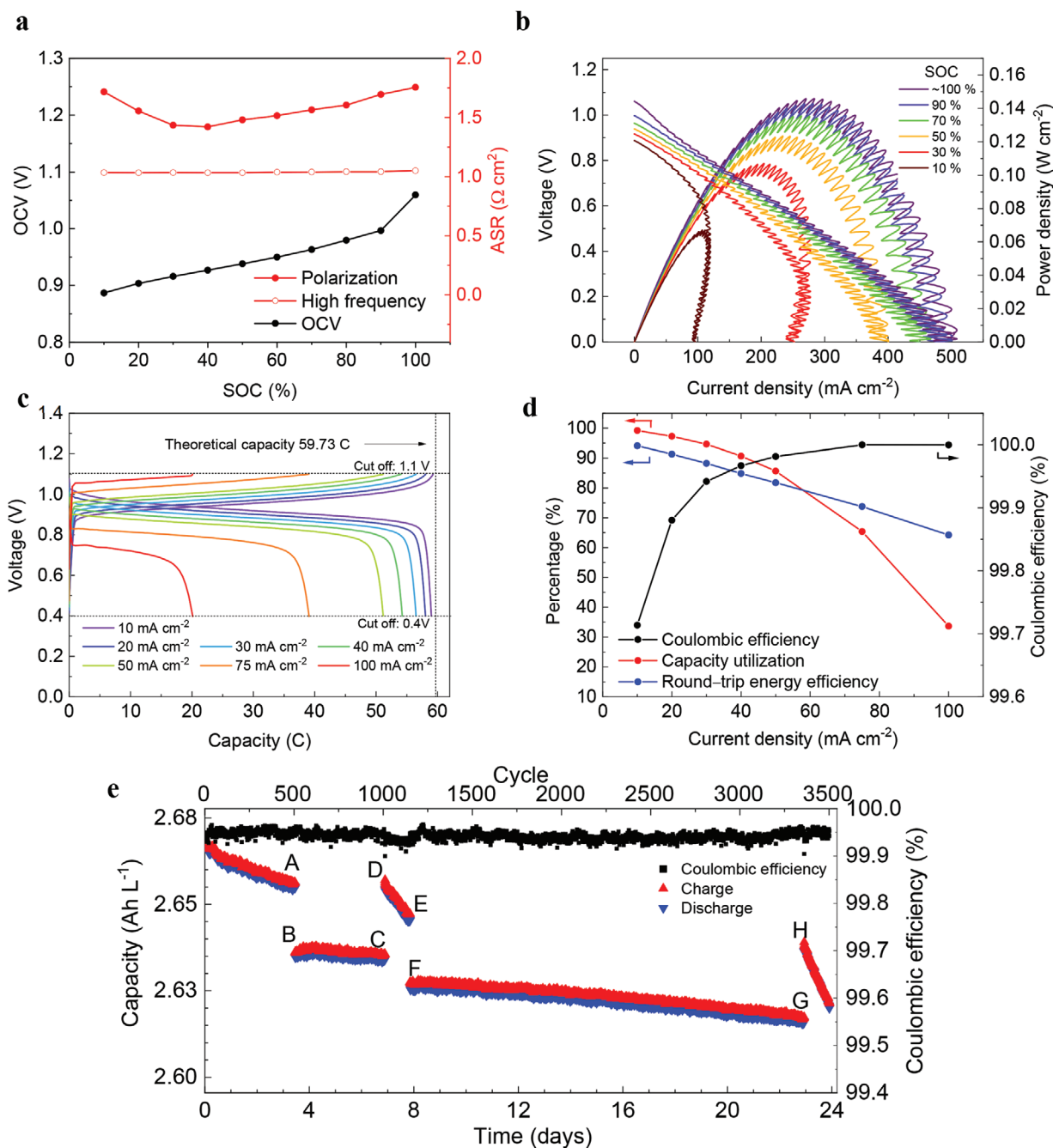
ADVANCED
SCIENCE NEWS
www.advancedsciencenews.com

ADVANCED
ENERGY
MATERIALS
www.advenergymat.de

Figure 4. Low-concentration flow battery performance. Electrolytes comprised 6.2 mL of 0.1 M BPP–Vi titrated with 1 M KOH in 1 M KCl to pH = 9 (negolyte) and 20 mL of 0.1 M $K_4Fe(CN)_6$ and 0.1 M $K_3Fe(CN)_6$ in 1 M KCl at pH = 9 (posolyte). a) OCV, high frequency and polarization ASR versus SOC. b) Cell voltage and power density during discharge at various SOC. Oscillations arise from peristaltic pumping. c) Galvanostatic charge and discharge curves at various current densities with 1.1 and 0.4 V cutoffs. The theoretical capacity is indicated by the vertical dashed line. d) Coulombic efficiency, capacity utilization and round-trip energy efficiency versus current density. e) Extended cycling at 40 mA cm^{-2} of the flow cell with same voltage cutoff for discharge (0.4 V) but different voltage cutoffs for charge. The voltage cutoff is 1.2 V for the periods, beginning to A, D to E, and H to the end. The voltage cutoff is 1.1 V for the periods B to C, and F to G. Stable cycling was observed when the lower charging cutoff was applied.

overpotentials, the accessible 2nd electron capacity is 47 times higher when 1.2 V is used compared to 1.1 V. The redox potential of the **BPP–Vi^{3-}/BPP–Vi^{4-}** couple is 400 mV lower than that of **BPP–Vi^{2-}/BPP–Vi^{3-}**, so we assume that the OCV of 50% SOC **BPP–Vi^{3-}/BPP–Vi^{4-}** versus $K_4Fe(CN)_6$/ $K_3Fe(CN)_6$ is 400 mV higher, i.e., 1.28 V. According to the Nernst equation

$$E = E^\circ - \frac{RT}{nF} \ln \frac{a_{BPP-Vi^{3-}} \, a_{[Fe(CN)_6]^{4-}}}{a_{BPP-Vi^{4-}} \, a_{[Fe(CN)_6]^{3-}}} \qquad (1)$$

where E is the cell potential, E° is the cell OCV at 50% SOC, R is the universal gas constant, T is the absolute temperature (298 K),

n is the number of electrons transferred (1), F is the Faraday constant and a refers to the activity of each species. Assuming dilute solution conditions implies

$$\frac{a_{BPP-Vi^{3-}}}{a_{BPP-Vi^{4-}}} = \frac{C_{BPP-Vi^{3-}}}{C_{BPP-Vi^{4-}}} \quad \text{and} \quad \frac{a_{[Fe(CN)_6]^{4-}}}{a_{[Fe(CN)_6]^{3-}}} = \frac{C_{[Fe(CN)_6]^{4-}}}{C_{[Fe(CN)_6]^{3-}}} \tag{2}$$

where C refers to the concentration of each species. After the full reduction of **BPP–Vi^{2-}** to **BPP–Vi^{3-}**, accompanied by oxidation of ferrocyanide to ferricyanide, the concentration of posolyte species changes to the following

$$C_{[Fe(CN)_6]^{4-}} = \frac{(0.02L \times 0.1M) - (0.006\,L \times 0.1M)}{0.02L} = 0.07M \tag{3}$$

$$C_{[Fe(CN)_6]^{3-}} = \frac{(0.02L \times 0.1M) + (0.006\,L \times 0.1\,M)}{0.02L} = 0.07M \tag{4}$$

When the applied potential E is 1.1 V, assuming $E°$ is 1.28 V, using equations Equation (1) to Equation (4), and applying the constraint

$$C_{BPP-Vi^{3-}} + C_{BPP-Vi^{4-}} = 0.1\,M \tag{5}$$

we deduce that $C_{BPP-Vio^{4-}} = 0.00009\,M$ and $C_{BPP-Vio^{3-}} = 0.09991\,M$. So the accessible **BPP–Vi^{4-}** amount is around 0.009%. When 1.2 V is applied, using the same equations, 0.42% **BPP–Vi^{4-}** can be accessed, which is 47 times higher than the accessed amount when 1.1 V is applied. The actual accessed percentage of **BPP–Vi^{4-}** is likely less than these amounts due to different types of overpotentials from DC–ASR at the currect cutoff value of 2 mA cm^{-2}, but the calculation shows that a significantly larger amount of **BPP–Vi^{4-}** is created when 1.2 V is applied. It is not very surprising that overcharging can cause capacity fade, as previous work shows that overcharging of anthraquinone, forming anthrone, is the dominant cause of capacity fade in an anthraquinone based flow battery.[31] We hypothesize that the fast degradation of the doubly reduced **BPP–Vi^{4-}**, which is consistent with the symmetric cell cycling of the **BPP–Vi^{3-}/BPP–Vi^{4-}** couple shown in Figure 4e, is the major source of capacity fade in all of our cells. To exploit the high solubility of **BPP–Vi**, we constructed a full cell with a concentrated negolyte comprising 5 mL 1.0 M **BPP–Vi** as the capacity-limiting side and posolyte comprising 20 mL of 0.5 M K$_4$Fe(CN)$_6$ /0.5 M Na$_4$Fe(CN)$_6$ with 0.1 M K$_3$Fe(CN)$_6$ as the non-capacity-limiting side. Over the 32 days of cell operation, we cannot report a conclusive fade rate because of the fluctuating capacity and the low accessed capacity (Figure S14, Supporting Information). We identify two potential reasons for the low accessed capacity: 1. the titration of saturated **BPP–Vi** with 10 M KOH, which may cleave the C–N bond of **BPP–Vi** and 2. the decomposition product clogging electrodes, which raises cell resistance. To avoid the issue caused by titration with strong base, a milder base, NH$_4$OH, was used. Even at 14 M, the ammonium hydroxide solution has a pH around 12. Indeed > 99.5% capacity utilization (**Figure 5**c,d) was achieved in a cell with 6.2 mL 1 M **BPP–Vi** tirated with NH$_4$OH as negolyte and 40 mL 0.3 M K$_4$Fe(CN)$_6$/0.3 M K$_3$Fe(CN)$_6$ in 2 M NH$_4$Cl as posolyte during galvanostatic cycling with potentiostatic holds at the

end. A 5 mA cm^{-2} current cutoff to a potentiostatic hold was imposed as soon as the voltage cutoffs were reached. Although the AC-ASR was higher due to low water activity in the membrane, polarization experiments across 10% to 90% SOC do not exhibit higher DC-ASR compared to the low concentration case (Figure 5a). The OCV at 50% SOC is 0.88 V, which is slightly lower than that of the 0.1 M cell and is likely influenced by a subtle effect of different supporting electrolytes. The peak power was achieved at 100% SOC with a value of 0.143 W cm^{-2} (Figure 5b). Galvanostatic cycling from 10 to 150 mA cm^{-2} show that close to 80% capacity utilization and 70% round trip energy efficiency can be realized at 100 mA cm^{-2} (Figure 5c,d). The extended cycling of this cell demonstrates a fade rate of 0.016% per day or 0.00069% per cycle (Figure 5e). When pairing with an equivalent volume of 1 M ferrocyanide, either with mixed K$^+$/Na$^+$ or NH$_4^+$ counterion, the **BPP–Vi** based flow cell should have an energy density of 11.8 Wh L^{-1}. Thus, this flow battery chemistry is operable at pH = 9 with extremely high electrolyte stability, extremely low electrolyte permeation, and reasonable power and energy densities.

The reduction potential of **BPP–Vi** at pH = 9 is 100 mV more negative than that of BTMAP-Vi and 10 mV more negative than that of MV (Figure S20, Supporting Information). Yet the extremely high cycling stability of the **BPP–Vi** full cell is on par with that of the BTMAP-Vi cell, and their capacity fade rates are two order of magnitude lower than that of a MV cell. The coexistence of low reduction potential and high stability in viologens is encouraging because this is an attribute that appears to be lacking in anthraquinones. Goulet, Tong et al. demonstrated that anthraquinones with lower reduction potential are more susceptible to irreversible decomposition through anthrone/bianthrone formation.[31] Although the decomposition mechanism of viologens is still under study, the absence of potential-stability correlation in such species suggests there are opportunities for developing a stable viologen with reduction potential close to the solvent stability window.

Although **BPP–Vi** has the most negative reduction potential among all viologen derivatives applied in aqueous flow batteries to date, the cell voltage is relatively low compared to many other flow batteries, including vanadium, phenazine, and some quinone-based chemistries.[11] Several directions are under study to raise the cell voltage of viologen-based flow batteries. For example, several groups have used (2,2,6,6-Tetramethylpiperidin-1-yl)oxyl or (2,2,6,6-tetramethylpiperidin-1-yl)oxidanyl (TEMPO) as posolyte.[18,24,29] We designed 4,4′-(3-sulfopropyl)amino)-(2,2,6,6-Tetramethylpiperidin-1-yl)oxyl (S–TEMPO), employing the same multi–negative charge concept as BPP–Vi; pairing S–TEMPO with BPP–Vi gives a potential difference of 1.3 V (Figure S10, Supporting Information). The cell performance of this pair is under study. Another method to further raise the cell potential is to further decrease the reduction potential of viologens. While the focus of our present work has been the development and performance of **BPP–Vi**, we additionally present preliminary results on 2,2′-methyl-substituted viologen species, illustrating substitutions that can further lower the reduction potential of viologens. **Figure 6**a–c shows that the 2,3′-dimethyl-1,1′-bis(3-phosphonopropyl)-[4,4′-bipyridine]-1,1′-diiium dibromide (**BPP–mVi**), 3,3′-(2,3′-dimethyl-[4,4′-bipyridine]-1,1′-diium-1,1′-diyl)bis(propane-1-sulfonate)
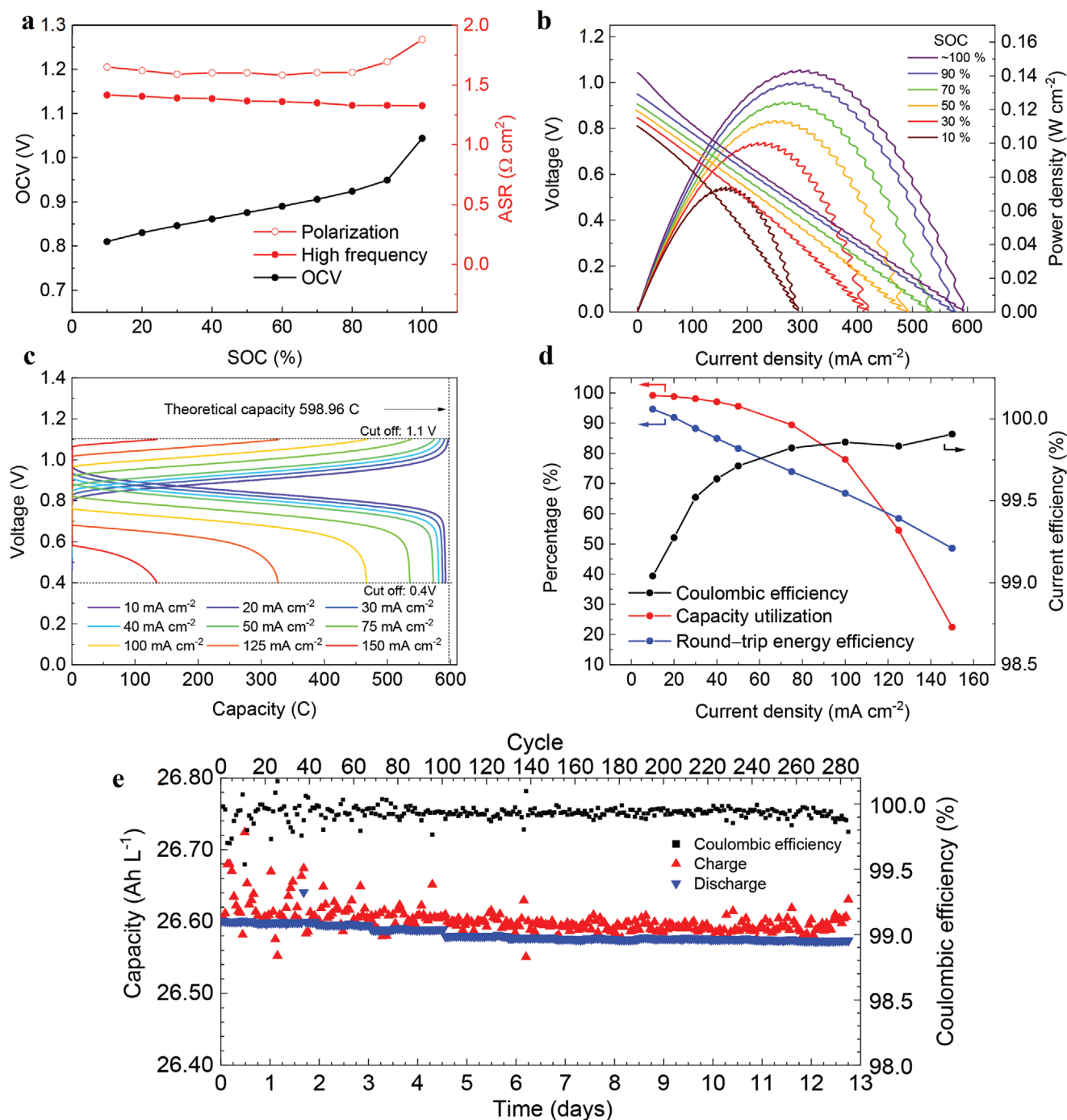
Figure 5. High-concentration flow battery performance. Electrolytes comprised 6.2 mL of 1.0 M BPP–Vi titrated with 14 M NH$_4$OH to pH = 9 (negolyte) and 40 mL of 0.3 M K$_4$Fe(CN)$_6$ and 0.3 M K$_3$Fe(CN)$_6$ in 2 M NH$_4$Cl at pH = 9 (posolyte). a) OCV, high frequency and polarization AC-ASR versus SOC. b) Cell voltage and power density during discharge at various SOC. c) Galvanostatic charge and discharge curves at various current densities with 1.1 and 0.4 V cutoffs. The theoretical capacity is indicated by the vertical dashed line. d) Coulombic efficiency, capacity utilization and round trip energy efficiency versus current density. e) Extended cycling at 40 mA cm^{-2} of the flow cell with 1.1 V charging voltage.

(**BPS–mVi**), and 2,2′-dimethyl-1,1′-bis(3-(trimethylammonio) propyl)-[4,4′-bipyridine]-1,1′-diium tetrabromide (**BTMAP–mVi**), have reduction potentials that are 86, 77, and 95 mV, respectively, more negative than the corresponding unsubstituted molecules at pH = 8. Such modifications can increase the overall cell voltage by ≈10%, with corresponding increases in energy density and power density. Computational results show that when stronger electron-donating groups, such as methoxy groups, are installed, the reduction potential may be further lowered (Figure S20, Supporting Information). These developments, in light of the absence of the unfavorable potential-stability correlation in viologen derivatives, may lead
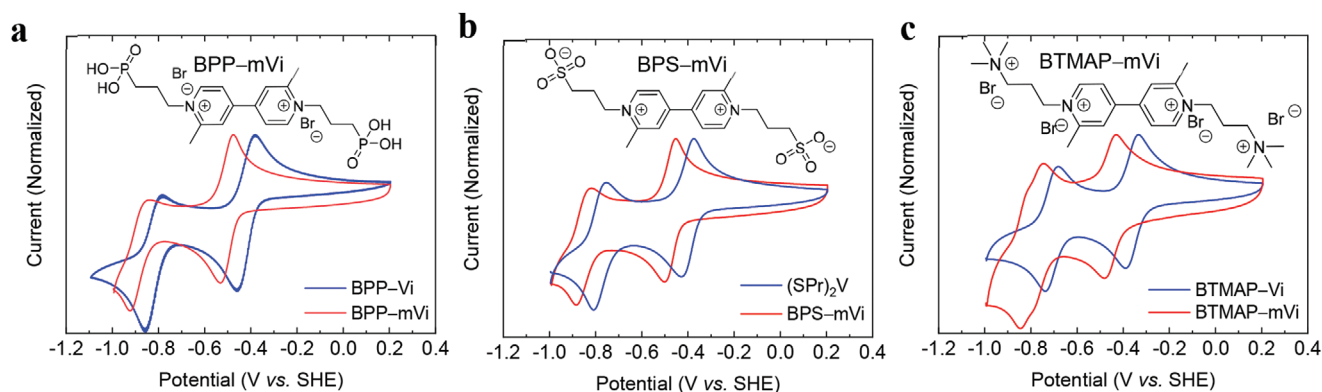
Figure 6. Comparison of CV of 2,2′-methylated funtionalized viologens and un-methylated viologens measured at pH = 8. The functional groups are 3-phosphonopropyl, propane-1-sulfonate and 3-(trimethylammonio)propyl in a), b) and c), respectively.

to higher-voltage ARFBs operating at near-neutral pH with the decadal lifetimes required for deployment on the grid.

3. Summary

We introduce **BPP–Vi** as a negolyte material for an ARFB that remains at near neutral pH throughout its charge-discharge cycle. The molecule is soluble up to 1.23 M and its reduction potential at pH = 9 of −0.462 V versus SHE is the most negative among viologens employed in flow batteries. The negative charges on both the oxidized and reduced forms of **BPP–Vi** help increase molecular stability and reduce permeation rates by enhancing electrostatic repulsion among **BPP–Vi** molecules and between molecules and the CEM. The measured permeability of **BPP–Vi** through a Fumasep E620 CEM is 2.2×10^{-13} cm^2 s^{-1}, which would result in ≈10% capacity fade due to **BPP–Vi** crossover in 1000 years. A symmetric cell at 0.2 M **BPP–Vi** and a full cell at 1 M **BPP–Vi** demonstrate extremely low capacity fade rates of 0.0023% per day and 0.016% per day, respectively. Capacity fade rate experiments and post-mortem NMR measurements support the interpretation that capacity decay occurs if one accesses a chemically unstable doubly reduced form. The high-concentration full cell exhibits a peak power density of 0.14 W cm^{-2} and a theoretical energy density of 11.8 W h L^{-1}, which might be further increased with the installation of electron donating groups on 2,2′ positions on the viologen core. This work introduces extremely stable, extremely low-permeating and low reduction potential redox active materials into near neutral ARFBs.

Supporting Information

Supporting Information is available from the Wiley Online Library or from the author.

Acknowledgements

Conflict of Interest

The authors declare no conflict of interest.

Keywords

[1] T. Stehly, D. Heimiller, G. Scott, *National Renewable Energy Laboratory* **2017**.
[2] P. Denholm, E. Ela, B. Kirby, M. Milligan, *National Renewable Energy Laboratory* **2010**.
[3] B. Obama, *Science* **2017**, *355*, 126.
[4] J. Rugolo, M. Aziz, *Energy Environ. Sci.* **2012**, *5*, 7151.
[5] B. Dunn, H. Kamath, J.-M. Tarascon, *Science* **2011**, *334*, 928.
[6] J. Luo, B. Hu, M. Hu, Y. Zhao, T. L. Liu, *ACS Energy Lett.* **2019**, *4*, 2220.
[7] https://electrek.co/2017/12/21/worlds-largest-battery-200mw-800mwh-vanadium-flow-battery-rongke-power/, "World's Largest Battery: 200MW/800 MWh Vanadium Flow Battery – Site Work Ongoing," accessed.
[8] https://global-sei.com/company/press/2018/12/prs102.html, accessed 2019/12/07.
[9] J. Winsberg, T. Hagemann, T. Janoschka, M. D. Hager, U. S. Schubert, *Angew. Chem., Int. Ed.* **2017**, *56*, 686.
[10] G. L. Soloveichik, *Chem. Rev.* **2015**, *115*, 11533.
[11] D. G. Kwabi, Y. Ji, M. J. Aziz, *Chem. Rev.* **2020**, https://doi.org/10.1021/acs.chemrev.9b00599.
[12] B. Huskinson, M. P. Marshak, C. Suh, S. Er, M. R. Gerhardt, C. J. Galvin, X. Chen, A. Aspuru-Guzik, R. G. Gordon, M. J. Aziz, *Nature* **2014**, *505*, 195.
[13] B. Hu, C. DeBruler, J. Moss, J. Luo, T. L. Liu, *ACS Energy Lett.* **2018**, *3*, 663.

ADVANCED
SCIENCE NEWS

www.advancedsciencenews.com

ADVANCED
ENERGY
MATERIALS

www.advenergymat.de

[14] K. Lin, Q. Chen, M. R. Gerhardt, L. Tong, S. B. Kim, L. Eisenach, A. W. Valle, D. Hardee, R. G. Gordon, M. J. Aziz, M. P. Marshak, *Science* **2015**, *349*, 1529.

[15] L. Tong, M.-A. Goulet, D. P. Tabor, E. F. Kerr, D. De Porcellinis, E. M. Fell, A. Aspuru-Guzik, R. G. Gordon, M. J. Aziz, *ACS Energy Lett.* **2019**, *4*, 1880.

[16] Z. J. Yang, L. C. Tong, D. P. Tabor, E. S. Beh, M. A. Goulet, D. De Porcellinis, A. Aspuru-Guzik, R. G. Gordon, M. J. Aziz, *Adv. Energy Mater.* **2018**, *8*, 1702056.

[17] D. G. Kwabi, K. Lin, Y. Ji, E. F. Kerr, M.-A. Goulet, D. De Porcellinis, D. P. Tabor, D. A. Pollack, A. Aspuru-Guzik, R. G. Gordon, M. J. Aziz, *Joule* **2018**, *2*, 1907.

[18] T. Janoschka, N. Martin, M. D. Hager, U. S. Schubert, *Angew. Chem., Int. Ed.* **2016**, *55*, 14427.

[19] Y. Ji, M. A. Goulet, D. A. Pollack, D. G. Kwabi, S. Jin, D. Porcellinis, E. F. Kerr, R. G. Gordon, M. J. Aziz, *Adv. Energy Mater.* **2019**, *9*, 1900039.

[20] E. S. Beh, D. De Porcellinis, R. L. Gracia, K. T. Xia, R. G. Gordon, M. J. Aziz, *ACS Energy Lett.* **2017**, *2*, 639.

[21] S. Jin, Y. Jing, D. G. Kwabi, Y. L. Ji, L. C. Tong, D. De Porcellinis, M. A. Goulet, D. A. Pollack, R. G. Gordon, M. J. Aziz, *ACS Energy Lett.* **2019**, *4*, 1342.

[22] J. Luo, A. Sam, B. Hu, C. DeBruler, X. L. Wei, W. Wang, T. L. Liu, *Nano Energy* **2017**, *42*, 215.

[23] B. Hu, C. DeBruler, Z. Rhodes, T. L. Liu, *J. Am. Chem. Soc.* **2017**, *139*, 1207.

[24] T. B. Liu, X. L. Wei, Z. M. Nie, V. Sprenkle, W. Wang, *Adv. Energy Mater.* **2016**, *6*, 1501449.

[25] J. Luo, B. Hu, C. Debruler, Y. J. Bi, Y. Zhao, B. Yuan, M. W. Hu, W. D. Wu, T. L. Liu, *Joule* **2019**, *3*, 149.

[26] J. Luo, W. D. Wu, C. Debruler, B. Hu, M. W. Hu, T. L. Liu, *J. Mater. Chem. A* **2019**, *7*, 9130.

[27] M. A. Goulet, M. J. Aziz, *J. Electrochem. Soc.* **2018**, *165*, A1466.

[28] M. Venturi, Q. G. Mulazzani, M. Z. Hoffman, *Radiat. Phys. Chem.* **1984**, *23*, 229.

[29] C. DeBruler, B. Hu, J. Moss, X. A. Liu, J. A. Luo, Y. J. Sun, T. L. Liu, *Chem* **2017**, *3*, 961.

[30] D. De Porcellinis, B. Mecheri, A. D'Epifanio, S. Licoccia, S. Granados-Focil, M. J. Aziz, *J. Electrochem. Soc.* **2018**, *165*, A1137.

[31] M. A. Goulet, L. Tong, D. A. Pollack, D. P. Tabor, S. A. Odom, A. Aspuru-Guzik, E. E. Kwan, R. G. Gordon, M. J. Aziz, *J. Am. Chem. Soc.* **2019**, *141*, 8014.

Supporting Information

Near Neutral pH Redox Flow Battery with Low Permeability and Long-Lifetime Phosphonated Viologen Active Species

Shijian Jin[†], Eric M. Fell[†], Lucia Vina-Lopez[†], Yan Jing[‡], P. Winston Michalak[§], Roy G. Gordon,[†,‡,]* and Michael J. Aziz[†,]*

† John A. Paulson School of Engineering and Applied Sciences, Harvard University, Cambridge, MA 02138, USA

‡ Department of Chemistry and Chemical Biology, Harvard University, Cambridge, MA 02138, USA

§ Harvard College, Cambridge, MA 02138, USA

* To whom correspondence should be addressed: gordon@chemistry.harvard.edu (Roy G. Gordon); maziz@harvard.edu (Michael J. Aziz).

Key words: redox flow battery, viologen, low permeability, neutral pH

predicted reduction potential for 2,2'-methoxy substituted viologens (labeled as -moVi), which are expected to have lower reduction potential compared to 2,2'-methyl substituted viologens (labeled as -mVi). The fact that the predicted reduction potential of 2,2'-methoxy substituted viologens is higher than 2,2'-methyl substituted viologens is likely caused by poor fitting, since the former do have lower calculated reduction potentials. The real reduction potential of the 2,2'-methoxy substituted viologens likely lie in the more negative region. The fitting can be improved by including more information of currently available viologens.
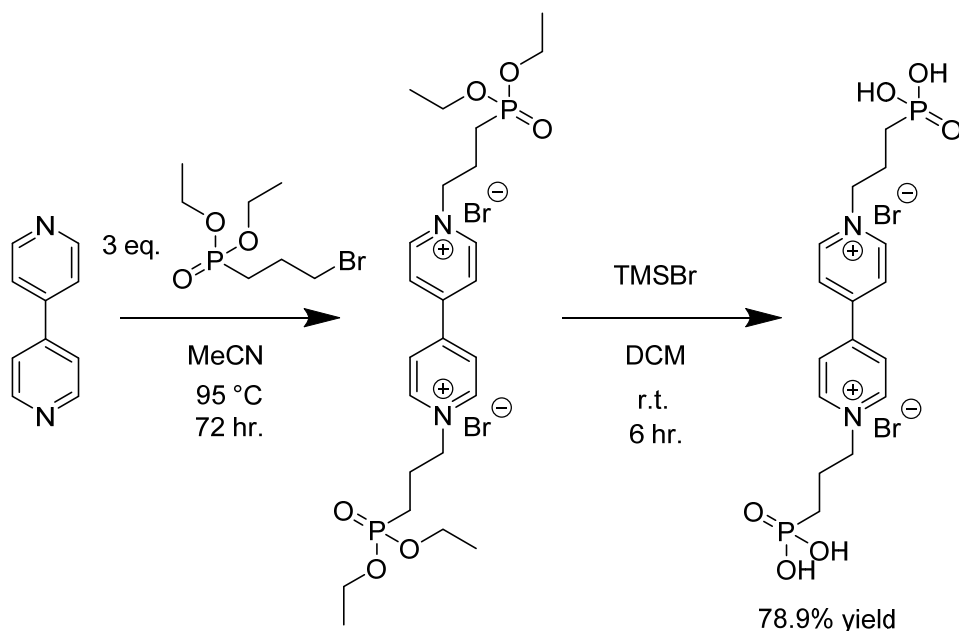
16
17

18 General Information

19

20 LC−MS was conducted on a Bruker microTOF-Q II mass spectrometer. All chemicals were
21 purchased from Sigma-Aldrich or Acros unless specified otherwise. All chemicals were used as
22 received unless specified otherwise.

23

24 Synthesis and Chemical Characterization

25

26
27 **Scheme S1. Synthesis of 1,1'-bis(3-phosphonopropyl)-[4,4'-bipyridine]-1,1'-diium dibromide**
28 **(BPP−Vi)**

29

30 *4,4'*-bipyridine (1 equiv.) was mixed with diethyl(3-bromopropyl)phosphonate (3 equiv.) in
31 anhydrous acetonitrile to achieve a 0.2 M bipyridine solution in a round bottom flask. The reaction
32 mixture was refluxed at 95 °C and stirred for 72 hours. The resulting slurry was filtered and the
33 precipitate was washed with acetonitrile and dried under vacuum to afford white solids 1,1'-bis(3-
34 (diethoxyphosphoryl)propyl)-[4,4'-bipyridine]-1,1'-diium dibromide (Yield: 78.9%).

35

36 1,1'-bis(3-(diethoxyphosphoryl)propyl)-[4,4'-bipyridine]-1,1'-diium (1 equiv.) dibromide was
37 mixed with bromotrimethylsilane (10 equiv.) under N$_2$ in dichloromethane to achieve a 0.1 M
38 viologen slurry in a round bottom flask. The reaction mixture was stirred overnight at room
39 temperature to give an orange solution. The orange solution was then quenched with excess
40 anhydrous isopropyl alcohol. The precipitate was filtered, dried and collected to give 98.9% yield
41 of 1,1'-bis(3-phosphonopropyl)-[4,4'-bipyridine]-1,1'-diium dibromide (**BPP−Vi**)

42

43 **(a) 1,1'-bis(3-(diethoxyphosphoryl)propyl)-[4,4'-bipyridine]-1,1'-diium dibromide**

44

45 ^{1}H NMR (500 MHz, D$_2$O) δ 9.16 (d, J = 6.0 Hz, 4H), 8.60 (d, J = 6.0 Hz, 4H), 4.80-4.87 (m, 4H),
46 4.13-4.22 (m, 8H) , 2.34-2.45 (m, 4H), 2.02-2.12 (m, 4H), 1.31-1.37 (m, 12H). ^{13}C NMR (125
47 MHz, D$_2$O) δ 151.44, 146.13, 127.18, 65.20, 60.49, 28.78, 23.77, 20.91, 20.16, 16.21.

5

(b) 1,1'-bis(3-phosphonopropyl)-[4,4'-bipyridine]-1,1'-diium dibromide (BPP–Vi)

^{1}H NMR (500 MHz, D$_2$O) δ 9.14 (d, J = 7.0, 4H), 7.66 (d, J = 7.0, 4H), 4.80-4.82 (m, 4H), 2.26-2.38 (m, 4H), 1.70-1.80 (m, 4H) ^{13}C NMR (125 MHz, D$_2$O) δ 150.9, 145.5, 129.7, 28.1, 23.7, 21.9.
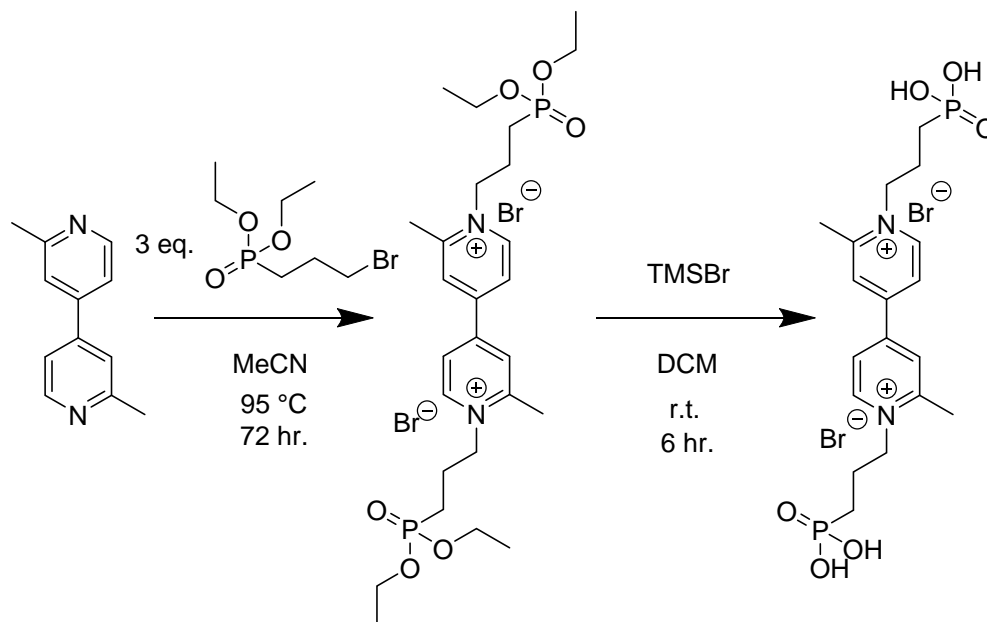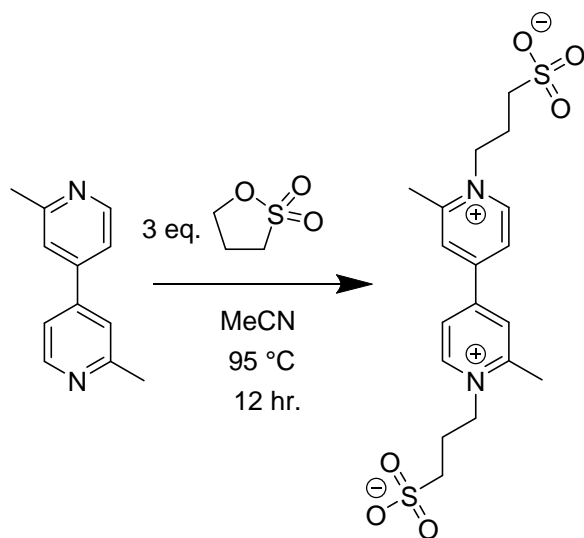

Scheme S2. Synthesis of BPP–mVi.

The synthetic procedure is the same as that of **BPP–Vi** except for replacing *4,4'*-bipyridine with *2,2'*-dimethyl-*4,4'*-bipyridine (purchased from Oakwood Product, Inc.). (two-step yield: 33%)

(c)   2,3'-dimethyl-1,1'-bis(3-phosphonopropyl)-[4,4'-bipyridine]-1,1'-diium   dibromide (BPP–mVi)

^{1}H NMR (500 MHz, D$_2$O) δ 9.00 (d, J = 7.0, 2H), 8.41 (s, 2H), 8.32 (d, J = 7.0, 2H), 4.74 (t, J =7.7, 4H), 2.99 (s, 6H), 2.19-2.32 (m, 4H), 1.86-1.95 (m, 4H) ^{13}C NMR (125 MHz, D$_2$O) δ 155.7, 150.2, 145.9, 131.4, 124.2, 23.9, 23.4, 21.9, 19.8

68
69
70 **Scheme S3. Synthesis of BPS−mVio.**
71
72 The synthetic procedure is the same as that of **BPP−mVio** except for replacing diethyl(3-
73 bromopropyl)phosphonate with 1,3-propane sultone. (Overall yield: 40%)
74
75 **(d)   3,3'-(2,3'-dimethyl-[4,4'-bipyridine]-1,1'-diium-1,1'-diyl)bis(propane-1-sulfonate)**
76 **(BPS−mVi)**
77
78 ^{1}H NMR (500 MHz, D$_2$O) δ 9.03 (d, J = 6.5, 2H), 8.43 (s, 2H), 8.33 (d, J = 6.5, 2H), 4.85 (t, J
79 =7.8, 4H), 3.12 (t, J = 7.0, 4H), 3.02 (s, 6H), 2.41-2.51 (m, 4H) ^{13}C NMR (125 MHz, D$_2$O) δ 156.6,
80 150.2, 146.8, 130.2, 122.4, 62.1, 48.1, 23.9, 19.8
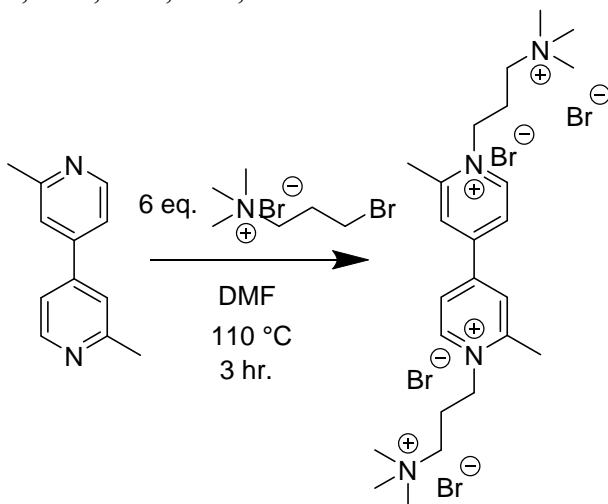

81
82 **Scheme S4. Synthesis of BTMAP−mVi.**
83
84 **(e)   2,2'-dimethyl-1,1'-bis(3-(trimethylammonio)propyl)-[4,4'-bipyridine]-1,1'-diium**
85 **tetrabromide**
86 *2,2'*-dimethyl-*4,4'*-bipyridine (1 equiv.)   and 3-bromo-N,N,N-trimethylpropan-1-aminium
87 bromide were suspended in anhydrous DMF to make 0.5 M bipyridine solution. All solids were

7

88 dissolved after the temperature was raised to 120 °C. The solution was stirred under heating for 3
89 hours, during which the solution turned orange and a large amount of precipitate formed. The
90 precipitate was filtered and then dissolved in a minimum amount of deionized water. Precipiation
91 occurred after an excess of anhydrous DMF was added to the aqueous solution. The pink
92 precipitate was then collected and identified to be **BTMAP–mVi** (Yield: 38%)
93
94 ^{1}H NMR (500 MHz, D$_2$O) δ 9.09 (d, J = 6.6, 2H), 8.51 (s, 2H), 8.41 (d, J = 6.5, 2H), 4.82 (t, J
95 =8.2, 4H), 3.64-3.70 (m, 4H), 3.24 (s, 18H), 3.05 (s, 6H), 2.57-2.66 (m, 4H) ^{13}C NMR (125 MHz,
96 D$_2$O) δ 155.9, 150.4, 146.0, 132.0, 125.2, 62.4, 56.8, 52.0, 23.4, 20.0,
97
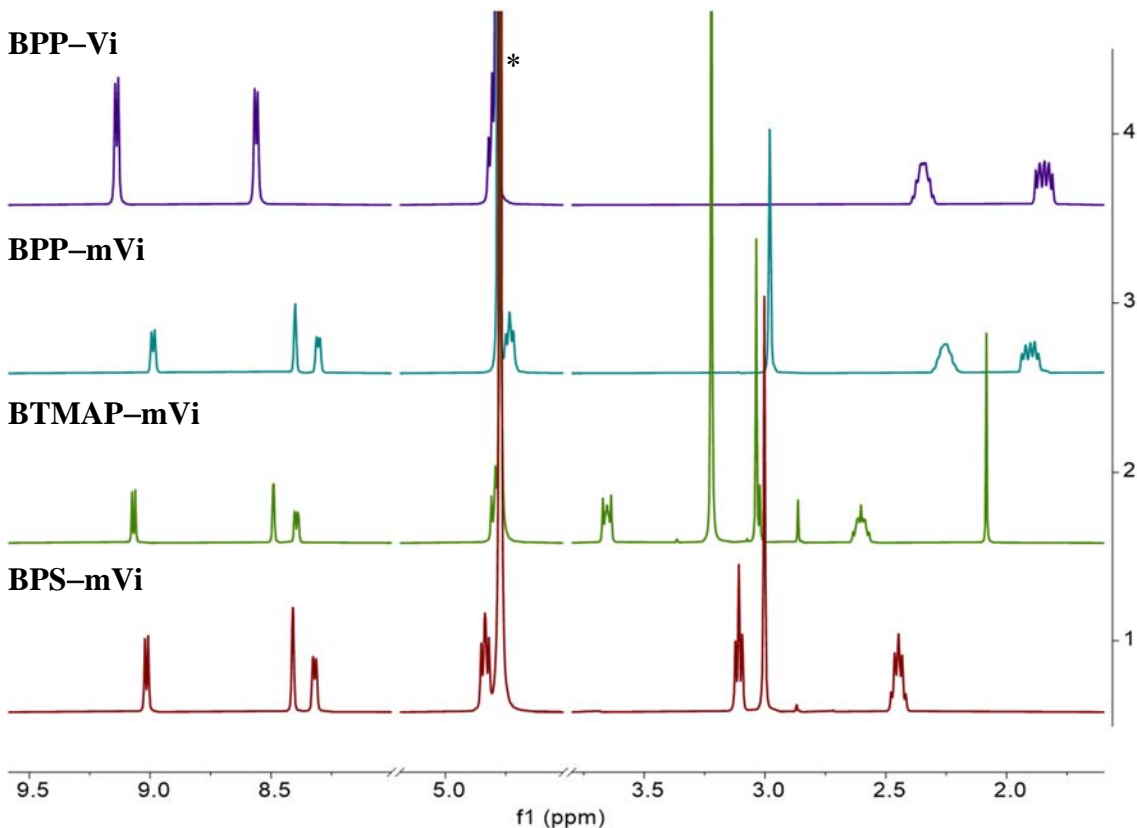
100 **Figure S1.** ^{1}H NMR spectra of **BPP–Vi**, **BPP–mVi**, **BPS–mVi** and **BTMAP–mVi** in D$_2$O. The
101 solvent peak labeled with * is from a trace amount of H$_2$O in D$_2$O solvent at 4.79 ppm.
102

BPP−Vi

BPP−mVi

BTMAP−mVi

BPS−mVi

f1 (ppm)
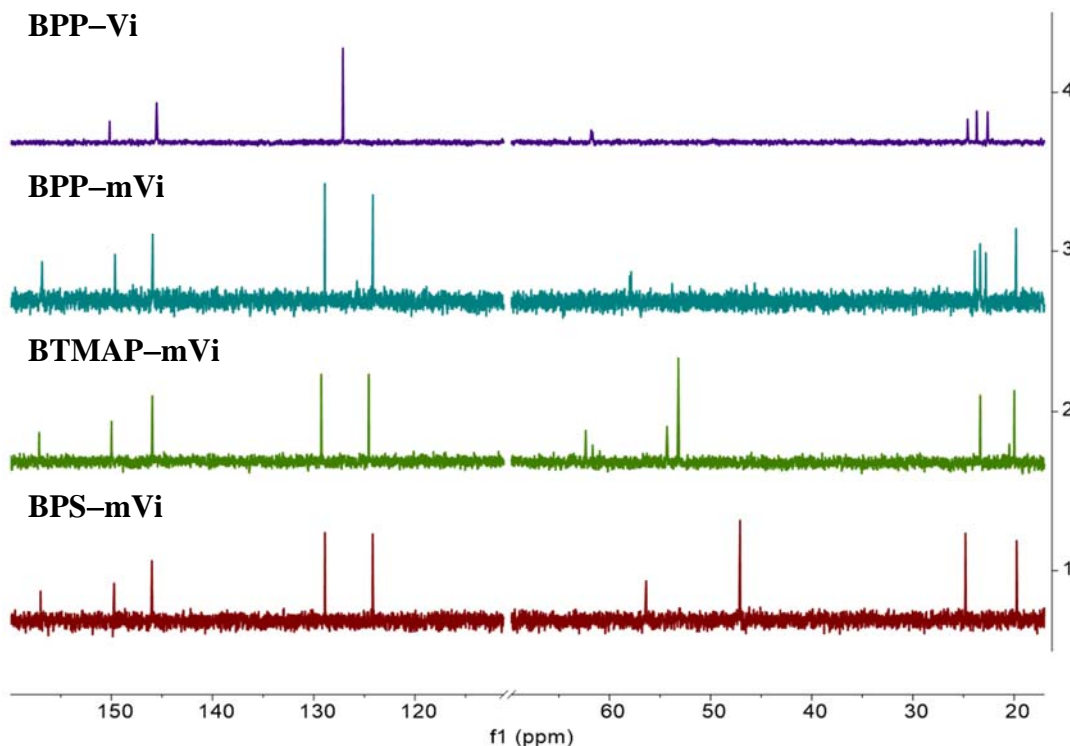
Figure S2. ^{13}C NMR spectra of **BPP−Vi**, **BPP−mVi**, **BPS−mVi** and **BTMAP−mVi** in D_2O.

(f) 4,4'-(3-sulfopropyl)amino)-(2,2,6,6-Tetramethylpiperidin-1-yl)oxyl (S-TEMPO)
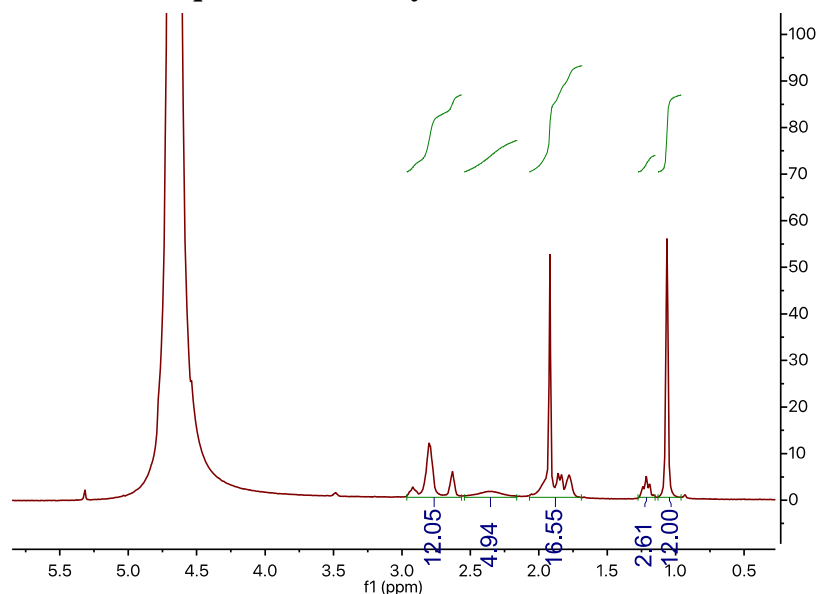
4-Amino TEMPO (1.71 g, 10 mmol) was dissolved in MeCN (50 mL), and then 1,3-Propane sultone (2.46 g, 20 mmol) was added to the solution. The mixture was stirred at room temperature overnight and became cloudy.[1]The mixture was filtered and was washed with MeCN (5 mL × 3) to give a pale pink solid (**S-TEMPO**) (Yield: 99%).
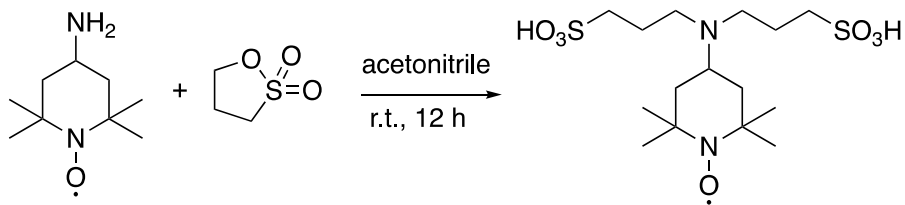
Scheme S5. Synthesis of S-TEMPO

9

S-TEMPO quenched with hydrazine

Figure S3 [superscript]1[/superscript]H NMR spectrum of nitrogen-subsititued **S-TEMPO** in D_2O. **S-TEMPO** was reduced by hydrazine prior to characterization.

Solubility Measurements

The solubility of **BPP−Vi** was measured using UV−Vis spectroscopy. A calibration line was obtained using the absorption peak at 265 nm of 5, 10, 20, 40 and 50 μM **BPP−Vi** solutions. An aliquot of saturated **BPP−Vi** solution was then diluted 50,000 times and then the absorption spectrum of the diluted solution was measured. The calculated solubility was 1.23 M. **Figure S4** shows the calibration line and the diluted saturated solution.
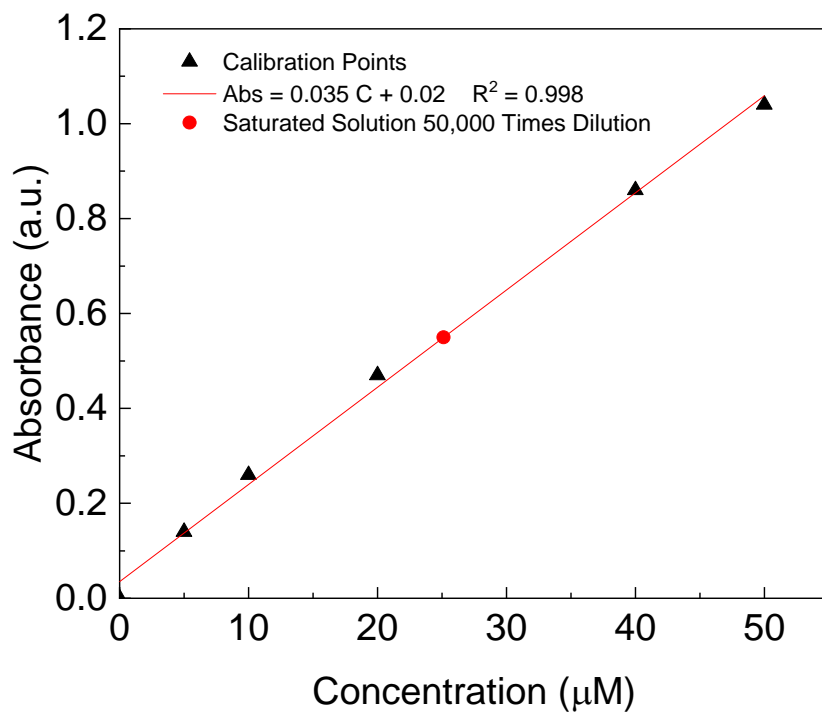
126
127 **Figure S4.** Calibration line and the measured solubility of **BPP–Vi**.
128
129 \

130

11
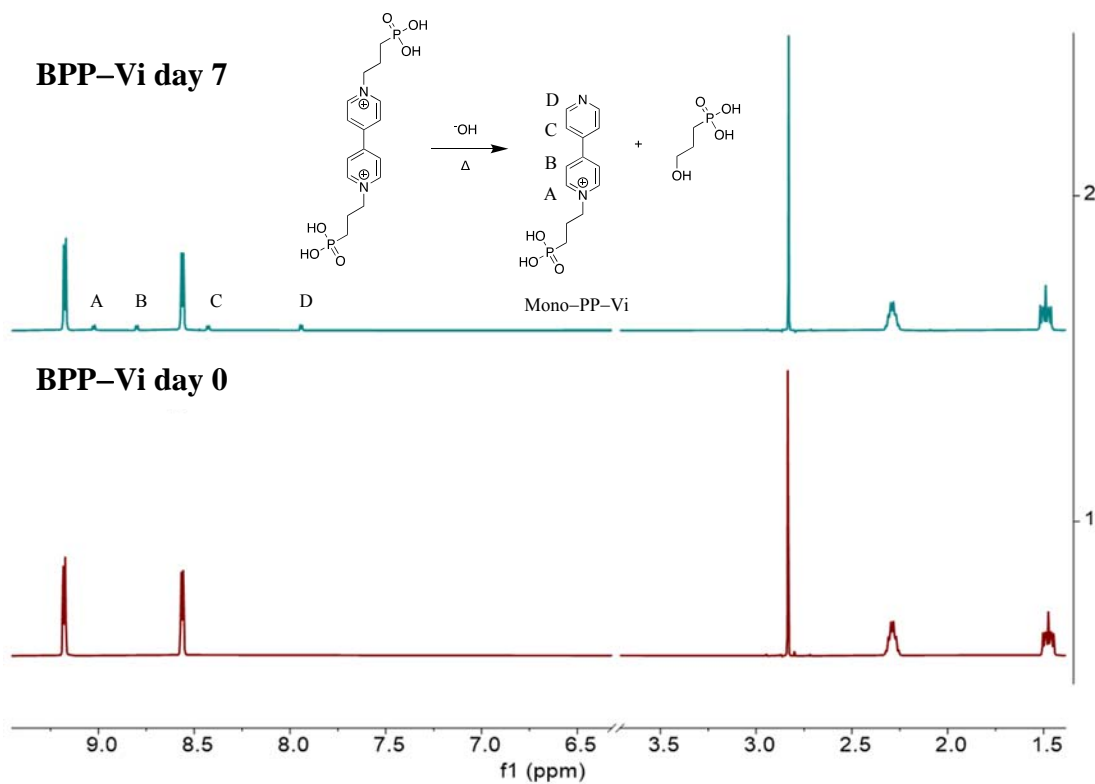
131   **Figure S5.** ^{1}H NMR spectra taken before and after the thermo-stability test. The peak at 2.85 ppm
132   is from the internal standard sodium methyl sulfate. After 7 days of storage at 65 °C, 5% of the
133   **BPP–Vi** degraded by dealkylation[4] and became 1-(3-phosphonopropyl)-[4,4'-bipyridin]-1-ium
134   bromide, or **Mono–PP–Vi**. The aromatic protons of **Mono–PP–Vi** are assigned to the peaks in
135   the NMR spectrum and the aliphatic protons of **Mono–PP–Vi** and the byproduct (3-
136   hydroxypropyl)phosphonic acid are hidden behind the peaks of **BPP–Vi**
137   <u>Electrochemical Characterization</u>
138
139   Glassy carbon (BASi MF-2012, 3.0mm diameter) was used as the working electrode for all three-
140   electrode CV tests. Rotating Disk Electrode experiments were conducted using a Pine Instruments
141   Modulated Speed Rotator AFMSRCE equipped with a 5 mm diameter glassy carbon working
142   electrode (Pine Instruments E5PK), a Ag/AgCl reference electrode (BASi MF-2052, pre-soaked
143   in 3 M NaCl solution), and a graphite counter electrode. Both CV and RDE tests were performed
144   using a Gamry Reference 3000 potentiostat. The diffusion coefficient of the oxidized form of
145   **BPP–Vi** was calculated using the Levich equation, which relates the mass-transport-limited
146   current to the number of electrons transferred (n), the area of the electrode (A), and the
147   concentration of redox-active species in the electrolyte (C), by plotting the mass-transport-limited
148   current against the square root of the rotation rate (Figure S8) with the following parameters: $n =$
149   1, $F = 96{,}485$ C mol^{-1}, $A = 0.196$ cm^2, $C = 5$ mM, $v = 1.08 \times 10^{-6}$ m^2 s^{-1} (the kinematic viscosity
150   of 1 M KCl)[2]. The resulting value of the diffusion coefficient of the oxidized form of **BPP–Vi** is
151   2.7×10^{-6} cm^2 s^{-1}. Koutecký–Levich analysis at low overpotentials can be extrapolated to infinite
152   rotation rate and fitted to the Butler–Volmer equation to give the standard rate constant $k_0 = 2.9 \times$
153   10^{-3} cm s^{-1} for the first reduction process.
154
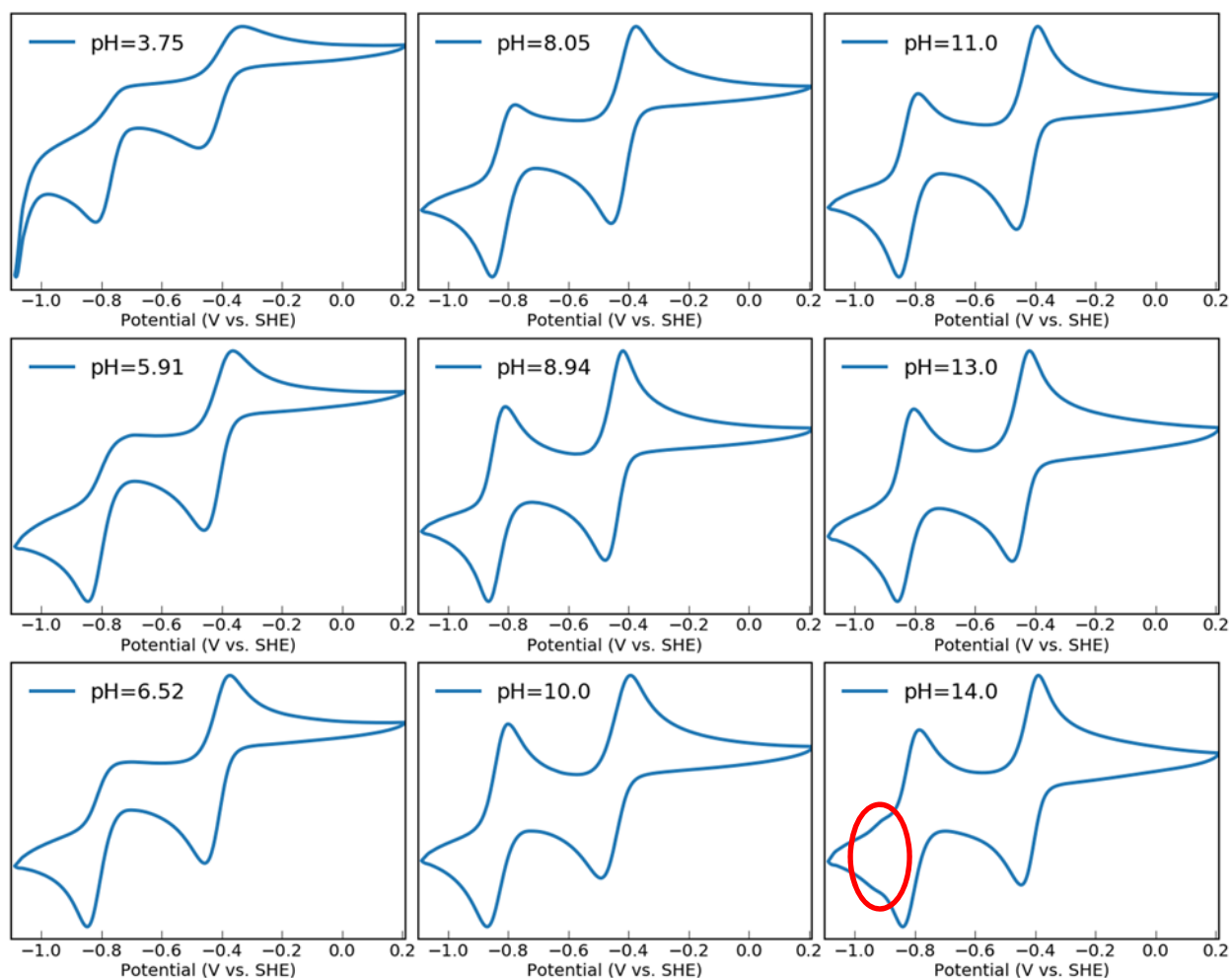
Figure S6. CV of **BPP–Vi** in 1 M KCl at different pH measured with 50 mV s⁻¹ scan rate and normalized to the height of the oxidative peak near −0.4 V *vs*. SHE. Optimal pH for electrochemistry is between pH = 9 to 13. The 1ˢᵗ reduction process is irreversible at pH 3.75 and decomposition takes place at pH = 14. The irreversibility at slightly acidic pH is caused by disproportionation-protonation side reations; at highly basic pH, concentrated hydroxides can cause dealkylation, thus resulting in molecular decomposition.[3,4]The circled region in pH = 14 subplot indicates the redox peaks from the decomposition product, i.e., Mono–BPP–Vi.

13
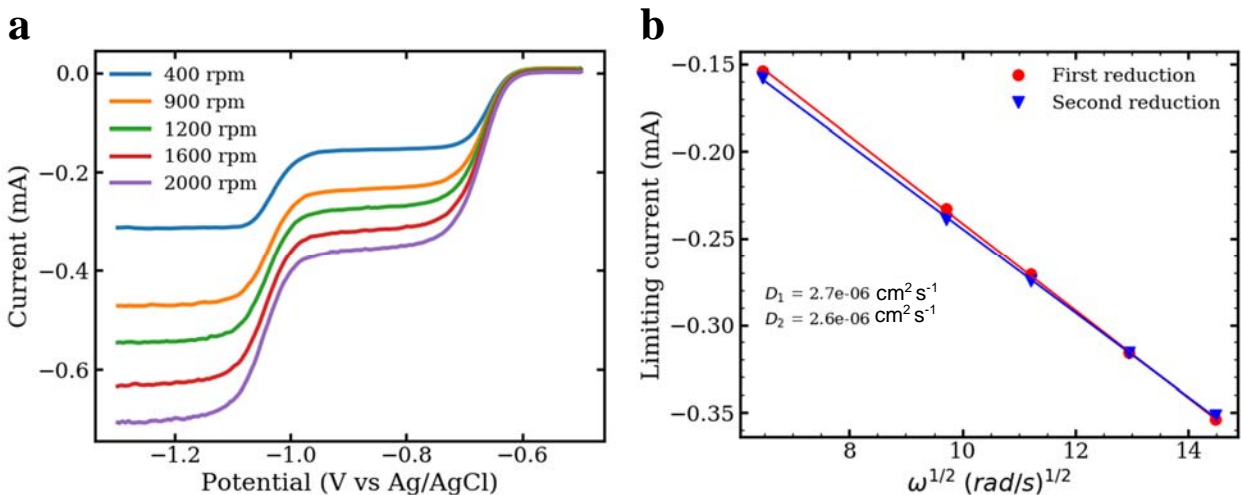
Figure S7. (a) RDE study of the reduction of 5 mM **BPP−Vi** in 1 M KCl at pH = 9 on a glassy carbon electrode at rotation rates between 400 and 2000 rpm. (b) Levich plot (limiting current *vs.* square root of rotation rate in rad s^{-1}) of 5 mM **BPP−Vi** in 1 M KCl at pH = 9. The slope yields a diffusion coefficient for the oxidized form of **BPP−Vi** of 2.7×10^{-6} cm^2 s^{-1}, and 2.6×10^{-6} cm^2 s^{-1} for the singly reduced form.
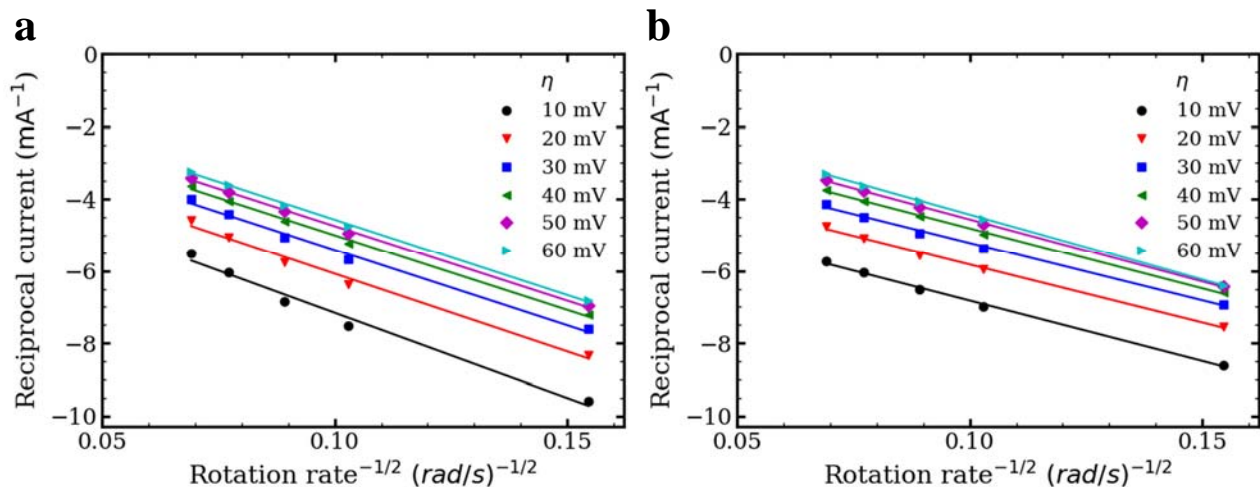
Figure S8. Koutecký−Levich analysis gives the values of mass-transport-independent currents at infinite rotation rate, for the (a) first reduction and (b) second reduction of **BPP−Vi**.

14
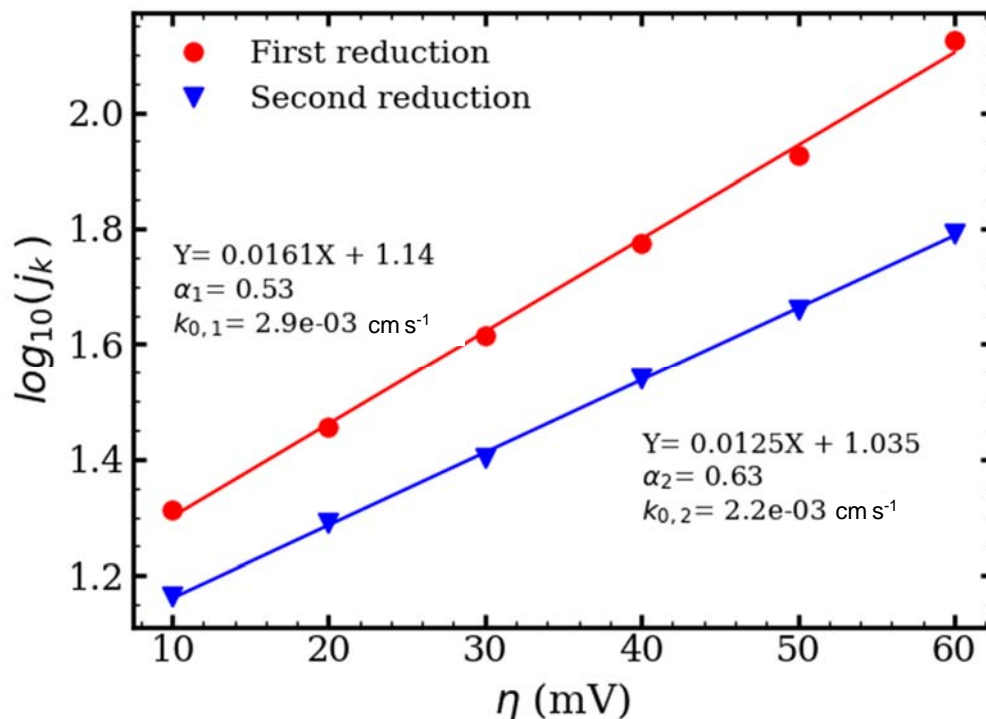
175
176 **Figure S9** Fit of Butler–Volmer equation. Constructed using the current response in the absence
177 of mass transport at low **BPP–Vi** reduction overpotentials; j_k is the current density extrapolated
178 from the zero-intercept of Figure S8. Analysis results in a standard rate constant k^0 of 2.9×10^{-3}
179 cm s^{-1} and 2.2×10^{-3} cm s^{-1} for the first reduction and the second reduction, respectively.
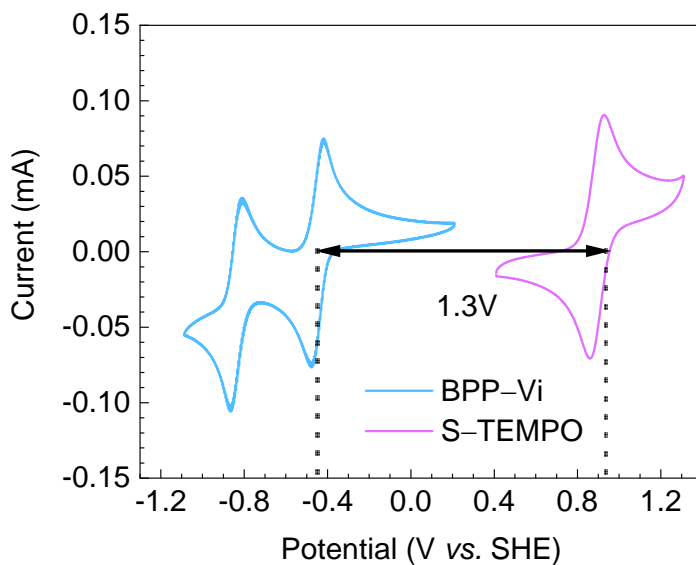
180
181 **Figure S10** Pairing **BPP–Vi** with **S-TEMPO** at pH = 9 can give >1.3 V equilibrium potential.
182

183

Determination of Viologen Derivatives Permeability through Nafion 212 and Fumasep E-620(K)
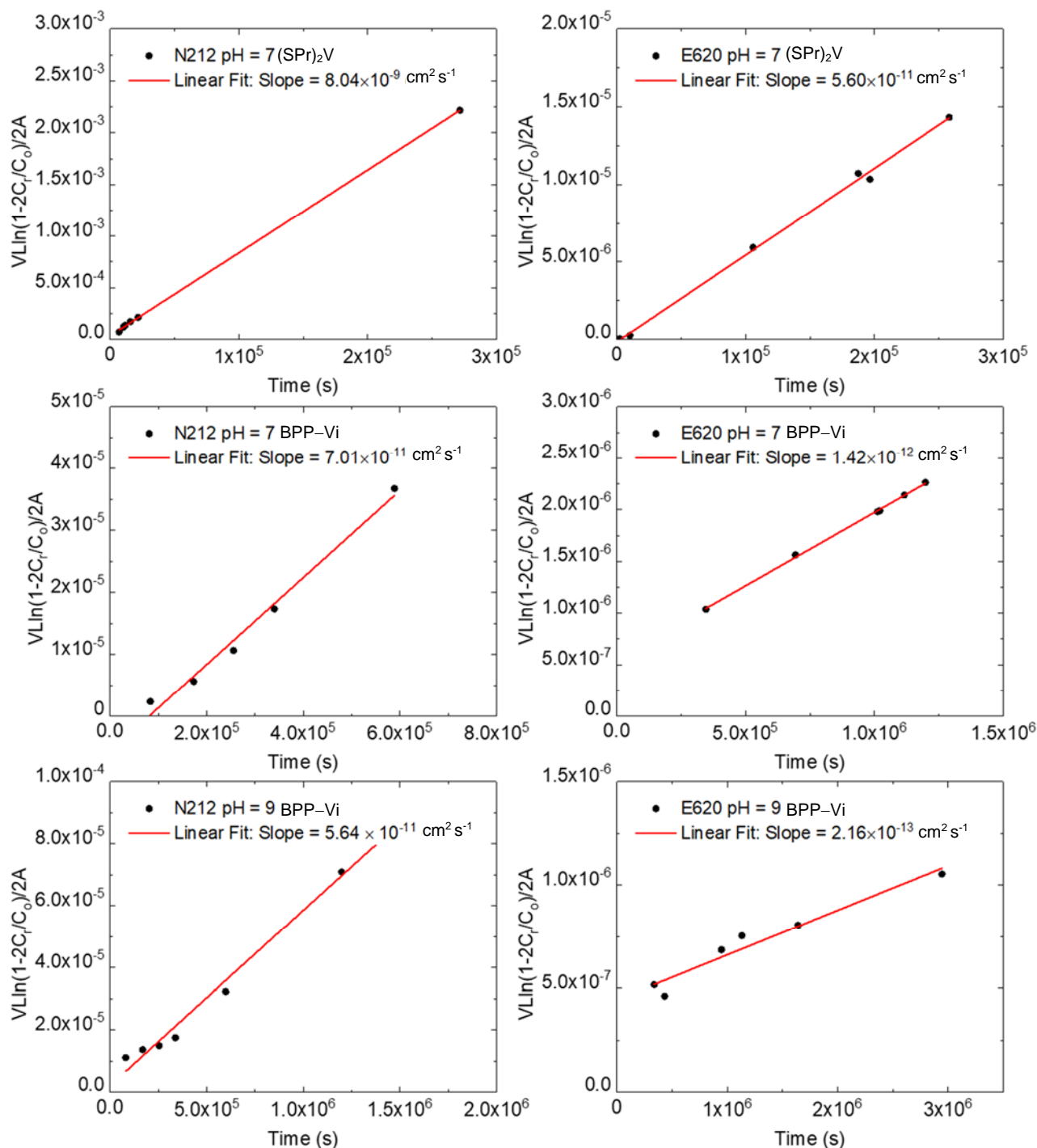
185
186 **Figure S**11. Permeabilities (slope of the fitted curve) of **BPP−Vi** and **(SPr)₂V** through Nafion 212
187 and Fumasep E620 membrane. The y−axis has the components from Eq. S1. The permeabilities
188 for **(SPr)₂V** through Nafion 212 and Fumasep E620 are 8.04×10^{-9} and 5.60×10^{-11} cm² s⁻¹,
189 respectively. The permeabilities for **BPP−Vi** through Nafion 212 and Fumasep E620 are 7.01×10^{-11} and 1.42×10^{-12} cm² s⁻¹, respectively at pH = 7, and 5.64×10^{-11} and 2.16×10^{-13} cm² s⁻¹ at pH = 9.

192 **Table S1.** Crossover of viologens across various membranes.[*]
193

Molecule	Structure	Charge in the oxidized/reduced form	Membrane	pH	Permeability [cm²s⁻¹]	Time to 10% capacity loss/years	Time to 50% capacity loss/years
MV[(a)]		+2/+1	Selemion DSV AEM	7	3.4×10^{-9}	0.3	2.1
BTMAP–Vi[(a)]		+4/+3	Selemion DSV AEM	7	6.7×10^{-10}	0.6	11
(SPr)₂V		0/−1	N212 CEM	7	8.0×10^{-9}	0.06	0.4
(SPr)₂V		0/−1	E620 CEM	7	5.6×10^{-11}	3.6	23
BPP–Vi		−2/−3	N212 CEM	7	7.0×10^{-11}	7.1	47
BPP–Vi		−2/−3	E620 CEM	7	1.4×10^{-12}	140	940
BPP–Vi		−2/−3	N212 CEM	9	5.6×10^{-11}	8.9	59
BPP–Vi		−2/−3	E620 CEM	9	2.2×10^{-13}	910	6000

194
195 [*]Assuming membrane is chemically stable
196 a. Ref. [4]
197
198

199   The permeability of **BPP−Vi** and 3,3'-([4,4'-bipyridine]-1,1'-diium-1,1'-diyl)bis(propane-1-
200   sulfonate) **(SPr)₂V** was measured across two types of cation exchange membranes, Nafion 212
201   and Fumasep E-620. A H-shaped crossover cell, with a donating side containing the redox active
202   species, a receiving side which was periodically monitored, and the membrane sandwiched
203   inbetween, was used.

204

205   A total of 6 cells were run. For (SPr)₂V cells, a solution of 0.1 M (SPr)₂V in 1 M KCl was placed
206   on the donating side, while the receiving side was filled with 1 M KCl at pH = 7. Two cells were
207   run under these conditions, one with Nafion 212 as a membrane, and the other with E620. The
208   cells were run for 1 and 2 days respectively. In the second case of **BPP−Vi**, the redox active species
209   was monitored at two different pH: pH = 7 and pH = 9. The donating sides were filled with 0.1 M
210   **BPP−Vi** in 1 M KCl (pH = 7 and pH = 9) and the receiving sides with 1.4 M KCl with pH = 7 and
211   pH = 9, respectively. Again, the crossover of the active species was monitored across two
212   membranes, Nafion 212 and E620, for each pH. For pH = 7 the cells ran for 6 and 13 days, for
213   each respective membrane, and for pH = 9 they ran for 16 and 34 days, respectively.

214

215   The cells were placed on a nutating table to keep the solutions continuously agitated and imitating
216   the fluid pumping that occurs in flow batteries. The initial electrolyte volume of both donating and
217   receiving side was made equal, and was periodically checked to ensure that it remained constant
218   throughout the experiment, to ensure no unwanted water crossover through the membrane.
219   Crossover of the redox active species was periodically monitored by taking a 500 μL aliquot from
220   the receiving side, and replacing it with fresh solution. This aliquot was diluted and run through
221   UV-visible spectrophotometry in order to determine the concentration of viologen that had crossed
222   over at that particular instance in time.

223

224   The permeability of each redox active species was calculated using Fick's Law,

225
$$P = \frac{\Delta \ln\left(1 - \frac{2C_r}{C_o}\right)\left(\frac{V_o L}{2A}\right)}{\Delta t} \qquad Eq.\,S1$$

226   where P is the permeability (cm² s⁻¹), C_r is the viologen concentration measured at the receiving
227   side at time t, C_0 is the initial concentration of viologen on the donating side, in our case 0.1 M. V_0
228   is the initial volume on either the receiving or donating sides, since they are equal. In this case 3.9
229   mL. A is the effective area of the membrane (0.713cm²), L is the thickness of the membrane (50
230   μM for Nafion 212 and 20 μM for E-620K) and Δt is time (s).

231

232   The expected time to 10% and 50% capacity loss is calculated according to the method presented
233   in our previous work from Beh *et al.*[4]

234

235   The detailed crossover measurements are shown in Figure S11 and summarized in Table S1.

236

237   <u>Flow Cell Measurements</u>

238

239   Flow battery experiments were constructed with cell hardware from Fuel Cell Tech. (Albuquerque,
240   NM), assembled into a zero-gap flow cell configuration, similar to a previous report.[5] Pyrosealed
241   POCO graphite flow plates with serpentine flow patterns were used for both electrodes. Each
242   electrode comprised a 5 cm² geometric surface area covered by a stack of four sheets of Sigracet

243   SGL 39AA porous carbon paper pre-baked in air for 24 h at 400 °C. The outer portion of the space
244   between the electrodes was gasketed by Viton sheets with the area over the electrodes cut out.
245   Torque applied during cell assembly was 60 lb-in on each of 8 bolts. Electrolytes were fed into the
246   cell through fluorinated ethylene propylene (FEP) tubing at a rate of 60 mL min^{-1}, controlled by
247   Cole-Parmer 6 Masterflex L/S peristaltic pumps. All cycling experiments were run inside a
248   nitrogen-filled glove box with an O_2 partial pressure less than 2 ppm. Polarization experiments
249   were run inside a nitrogen-filled glove bag with a nitrogen flow of 0.47 L min^{-1}. Cell polarization
250   measurements, impedance spectroscopy, and charge-discharge cycling were performed using a
251   Biologic VSP 300 potentiostat.
252
253   **Symmetric Cell Measurements**
254
255   Cycling stability of the **BPP–Vi** electrolyte was studied by the volumetrically unbalanced
256   compositionally symmetric cell method, previously described elsewhere.[6-8] For all symmetric cell
257   tests, a sheet of Nafion 117 (Ion Power) membrane served as the ion-selective membrane between
258   the carbon electrodes. Capacity limiting sides (CLS) contained 6 mL of electrolyte, while non-
259   capacity limiting sides (NCLS) contained 11 mL of electrolyte, both initially at 50% state-of-
260   charge (SOC) of the reduction process of interest. For symmetric cells investigating the first
261   reduction process, the starting 50% SOC mixture was composed of equal amounts oxidized
262   **BPP–Vi (BPP–Vi^{2-})** and singly reduced **BPP–Vi (BPP–Vi^{3-})**, whereas symmetric cells
263   investigating the second reduction process contained starting 50% SOC mixtures composed of
264   equal amounts of singly reduced **BPP–Vi(BPP–Vi^{3-})** and doubly reduced **BPP–Vi (BPP–Vi^{4-})**.
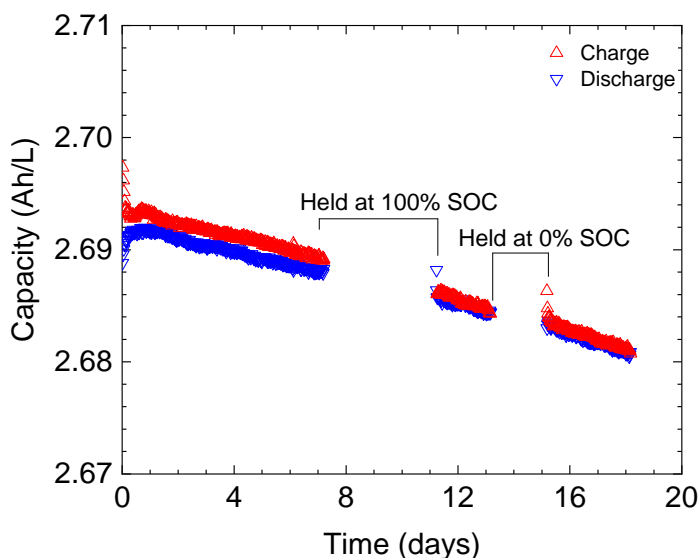
265
266   **Figure S12.** Extended unbalanced compositionally symmetric cell cycling of 0.1 M **BPP–Vi**.
267   Only the 1st electron is accessed.
268
269   **Full Cell Measurements**
270
271   Full cell cycling was performed with a Fumasep E-620(K) membrane due to its low permeability
272   to **BPP–Vi** and ferro/ferricyanide. To obtain the polarization curves, the cell was first charged to

273 the desired SOC and then polarized via linear sweep voltammetry at a rate of 100 mV s^{-1}. This
274 method was found to yield polarization curves very close to point-by-point galvanostatic holds,
275 yet imposes minimal perturbation to the SOC of the small-electrolyte-volume cell.
276 Electrochemical impedance spectroscopy (EIS) was performed at SOCs between 10 and 100% at
277 open-circuit potential with a 10 mV perturbation and with frequency ranging from 1 to 100,000
278 Hz. Three cells with varying negolyte and posolyte concentrations were studied.
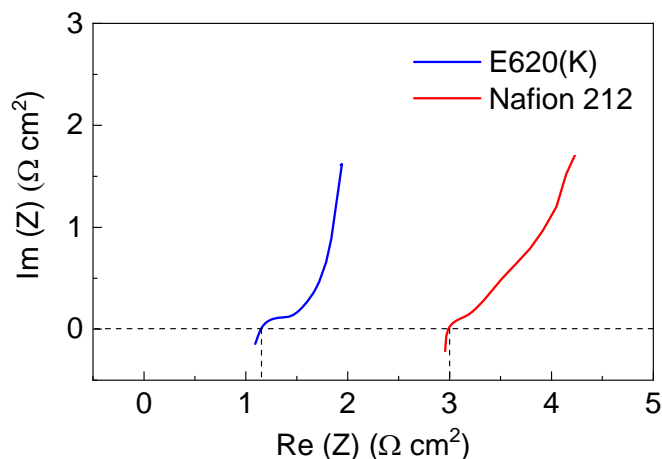
279
280 **Figure S13.** Nyquist plots of potentiostatic EIS measurements on 0.1 M full cell using E620(K)
281 and Nafion 212 CEM. The membrane resistance was determined at high frequency where the
282 imaginary impedence is 0. The resistance of E620(K) is ~ 1.1 Ω cm^2 and that of Nafion 212 is
283 3.0 Ω cm^2.
284
285 1. 0.1 M cell with K$^+$ counterion: The negolyte of the 0.1 M cell was prepared by dissolving
286   **BPP–Vi** (0.35 g, 0.62 mmol) and KCl (0.46 g, 6.2 mmol) into 3.7 mL deionized water,
287   followed by neutralization with 2.5 mL of 1 M KOH solution. Drops of 2 M KOH were
288   then added to the solution to achieve pH = 9. The posolyte of the 0.1 M cell was prepared
289   by dissolving K$_4$[Fe(CN)$_6$]·3H$_2$O (0.85 g, 2 mmol) and K$_3$[Fe(CN)$_6$]·6H$_2$O (0.26 g, 0.8
290   mmol) into 20 mL 1 M KCl to make a 0.1 M ferrocyanide 0.04 M ferricyanide solution. 0.5
291   mL of the negolyte solution was saved for further analysis. Extended cycling data are
292   shown in Figure S12.
293
294 2. 1 M cell with K$^+$/Na$^+$ counterion: The negolyte of the 1 M cell was prepared by dissolving
295   **BPP–Vi** (2.81 g, 5 mmol) into 2 mL DI water, followed by slow titration (0.05 mL at a
296   time) of 2 mL of 10 M KOH solution. The volume of the solution expanded to 5 mL to
297   achieve a 1 M **BPP–Vi** solution. Note that the solution becomes very dark due to
298   decomposition of some **BPP–Vi** molecules. The posolyte of the 1 M cell was prepared by
299   dissolving K$_4$[Fe(CN)$_6$]·3H$_2$O (4.22 g, 10 mmol), Na$_4$[Fe(CN)$_6$]·10H$_2$O (4.84 g, 10 mmol),
300   and K$_3$[Fe(CN)$_6$]·6H$_2$O (0.66 g, 2 mmol) into 20 mL DI water to make a 1 M ferrocyanide
301   and 0.1 M ferricyanide solution. The accessed capacity was only 80% compared to the
302   theoretical value because the negolyte was prepared by titrating a saturated **BPP–Vi**
303   solution with 10 M KOH. Titration was necessary to raise the pH from 1 to 9, but the high
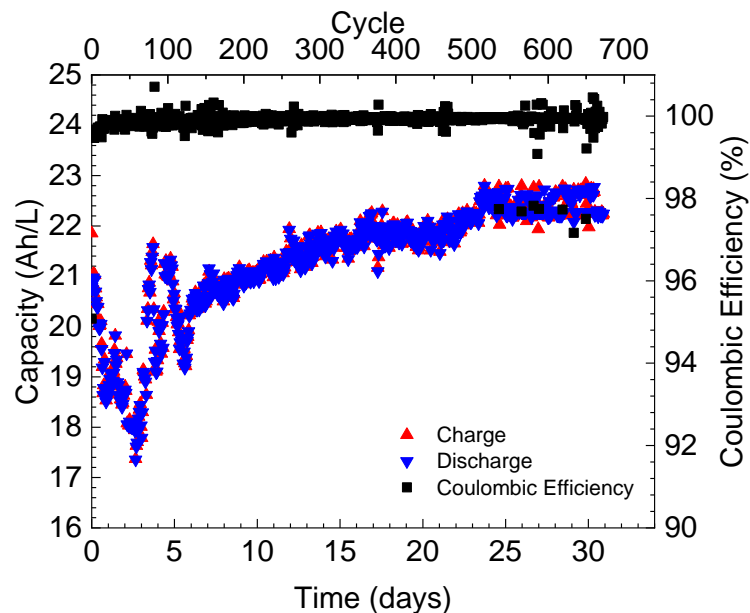304   alkalinity of the base also destroys **BPP–Vi** molecules.
305

Figure S14. Extended cycling of 1 M **BPP−Vi** titrated with 10 M KOH. Theoretical capacity of 1 M **BPP−Vi** electrolyte is 26.8 Ah L^{-1}. The accssed capacity is 85%.

3. 1 M cell with NH$_4^+$ counterion: The negolyte of the 1 M cell was prepared by dissolving **BPP−Vi** (3.5 g, 6.2 mmol) into 4 mL DI water, followed by titration of 1.7 mL of 14 M NH$_4$OH solution. More DI water was then added until the volume of the solution reached 6.2 mL to achieve a 1 M **BPP−Vi** solution. The solution color changed to light orange-brownish. Heat was released during the neutralization process. The posolyte of the 1 M cell was prepared by dissolving K$_4$[Fe(CN)$_6$]·3H$_2$O (5.06 g, 12 mmol), and K$_3$[Fe(CN)$_6$]·6H$_2$O (3.95 g, 12 mmol) into 40 mL of 2 M NH$_4$Cl solution to make a 0.3 M ferrocyanide and 0.3 M ferricyanide solution.

Post Cycling Analysis of **BPP−Vi**

321 A decomposition rate was hard to determine for the 1 M **BPP−Vi** symmetric cell cycling due to
322 the fluctuation of the data caused by insufficient electrolyte-mixing. To further analyze the post-
323 cycling material, NMR spectroscopy and LC-MS were conducted. Comparing the NMR spectra
324 before and after the 25-day 1 M **BPP−Vi** symmetric cell cycling, no new peak was observed
325 (**Figure S14**). The integration of the **BPP−Vi** peaks did not decrease either (**Figure S15–16**). Both
326 spectra suggest minimal decomposition during the cycling process.

BPP-Vi after 1 M symmetric cell cycling

BPP-Vi before 1 M symmetric cell cycling
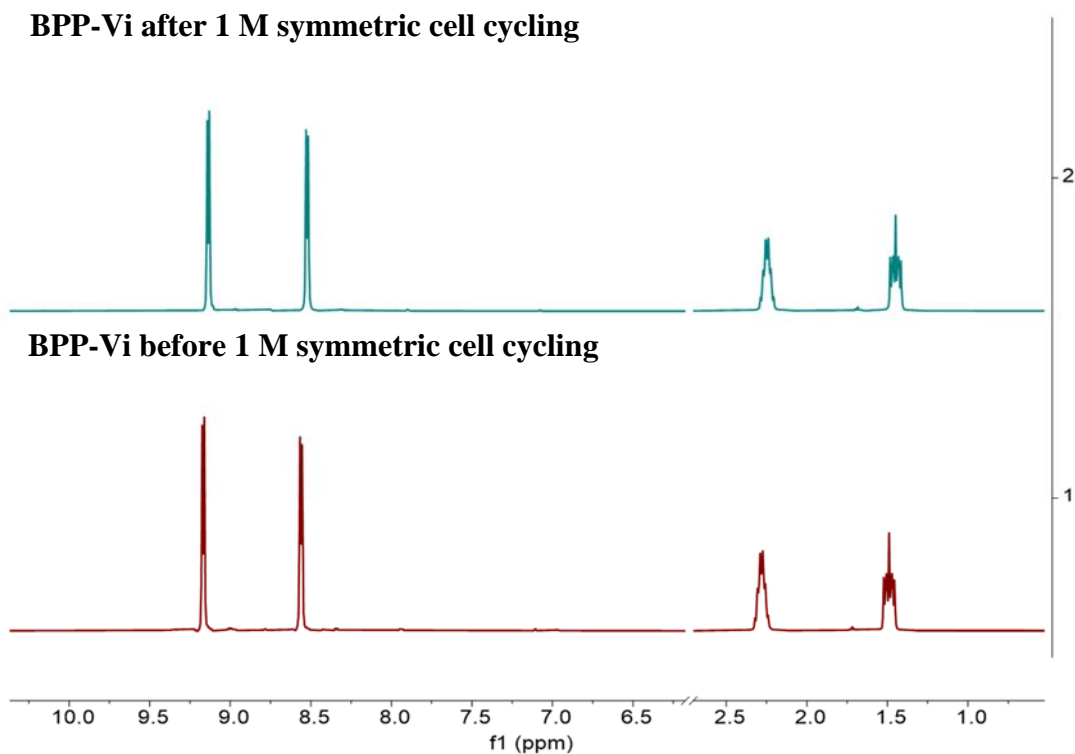
327
328 **Figure S15.** Stacked NMR spectra of 1 M **BPP−Vi** solution taken before and after the 25 days of
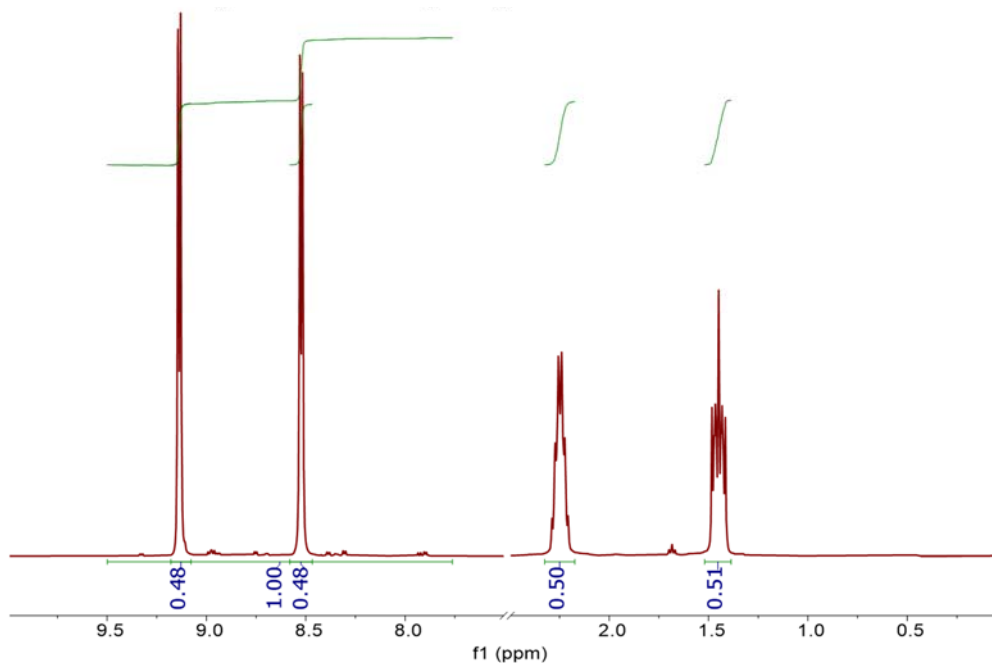329 the symmetric cell cycling. The integrations are shown in figure S15 and S16.

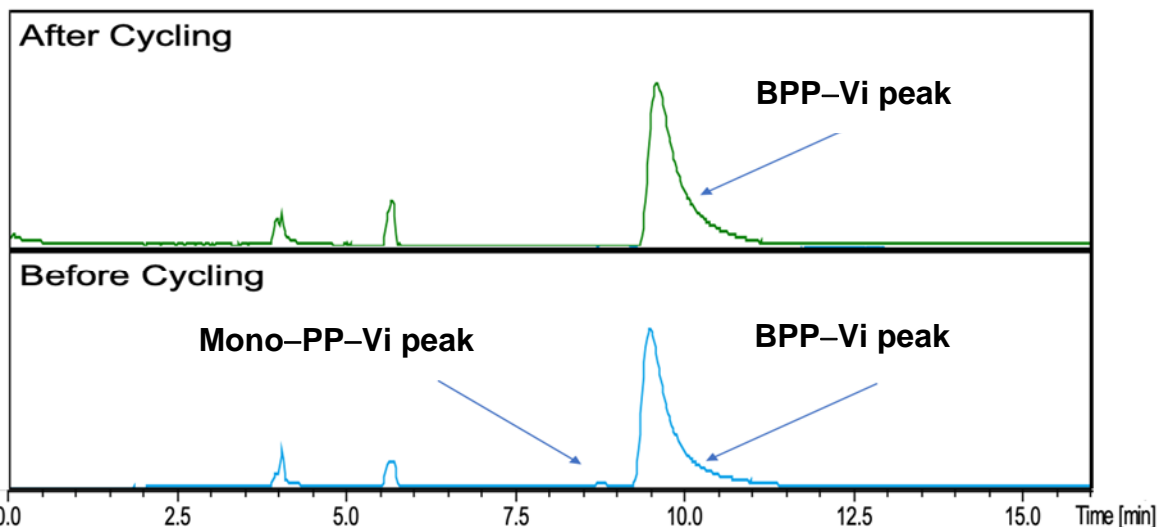**BPP-Vi before 1 M symmetric cell cycling**
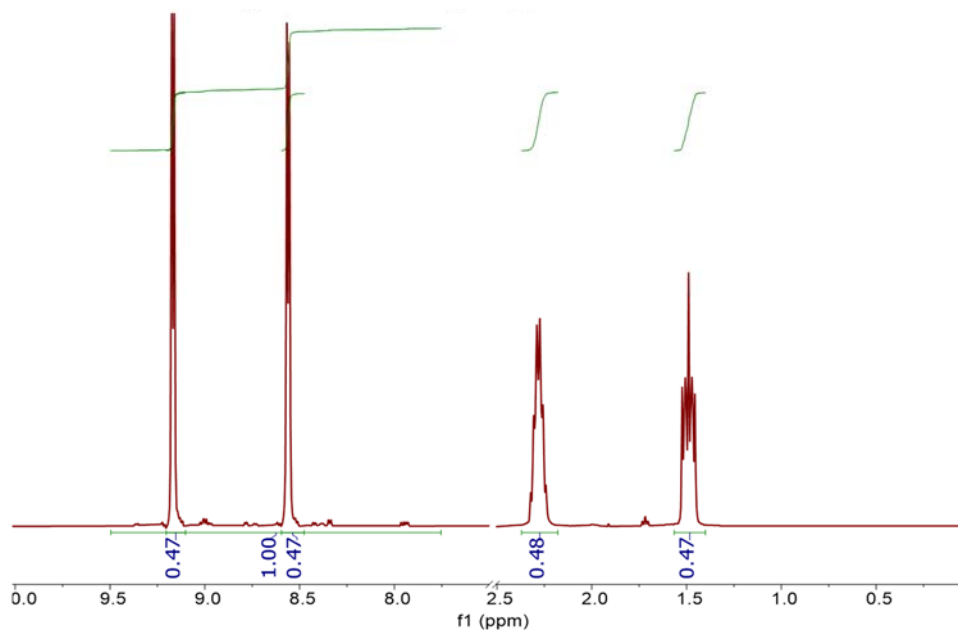
330
331
332 **Figure S16.** NMR spectrum taken before 1 M symmetric cell cycling. The NMR sample was
333 prepared by diluting 0.1 mL of 1 M **BPP−Vi** with 0.6 mL D$_2$O. The side peaks in the aromatic
334 region are decomposition products created during titration with 10 M KOH.
335

BPP-Vi after 1 M symmetric cell cycling

336
337
338 **Figure S17.** NMR spectrum taken after 25 days of 1 M symmetric cell cycling. The NMR sample
339 was prepared by diluting 0.1 mL of 1 M **BPP−Vi** with 0.6 mL D$_2$O. The integration of **BPP−Vi**
340 peaks does not decrease relative to the integration of the side peaks.

23

Figure S18. Liquid chromatography chromatograms of 1 M **BPP–Vi** solution taken before and after the 25 days of the symmetric cell cycling. The large peak at 9 min is attributed to **BPP–Vi**, whose mass-spectrum is shown in **Figure S14**. Peaks occurring before 7.5 min are contaminants from the column. No new peak was observed in the post-cycling sample. The small peak associated with Mono–PP–Vi disappeared in the post-cycling sample, but this is not relevant to **BPP–Vi** decomposition.
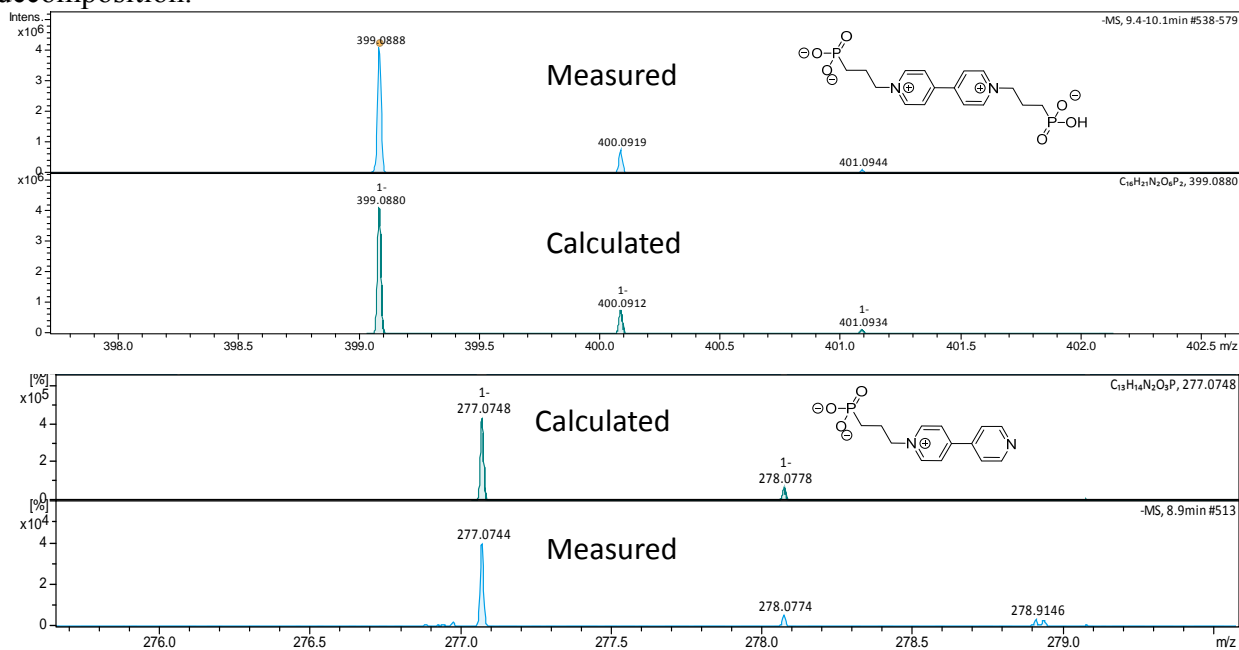
Figure S19. Mass-spec spectra of **BPP–Vi** (top) detected at 10.3 minutes and Mono–**BPP–Vi** (bottom) detected at 8.9 minutes. Both detected and theoretical masses are shown.

<u>DFT Calculation of Viologens</u>

Structural optimization and energy calculations of the optimized structures were performed using Gaussian 16, B3LYP/6-31G(d) method/basis-set with Solvation Model based on Density (SMD).

24
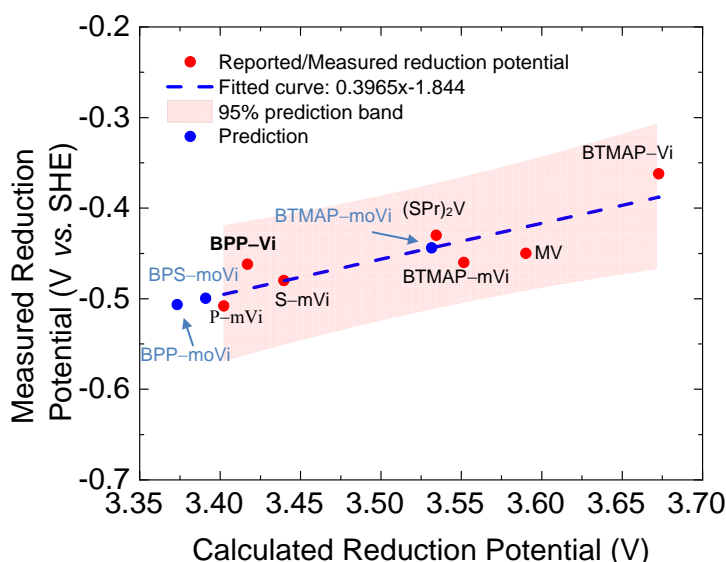
Figure S20. DFT calculation of the electronic energy of viologens. The calibration curve is fitted with the six available viologens, whose measured reduction potential values are adopted from most negative values reported by literature or measured in this work, and the red band is a 95% prediction band.[4,9,10] The three blue points are the predicted reduction potential for 2,2'-methoxy substituted viologens (labeled as -moVi), which are expected to have lower reduction potential compared to 2,2'-methyl substituted viologens (labeled as -mVi). The fact that the predicted reduction potential of 2,2'-methoxy substituted viologens is higher than 2,2'-methyl substituted viologens is likely caused by poor fitting, since the former do have lower calculated reduction potentials. The real reduction potential of the 2,2'-methoxy substituted viologens likely lie in the more negative region. The fitting can be improved by including more information of currently available viologens.

Supplementary References

[1]K.V.B. Ba-Tian Chen, Rachid Sougrat, Valentin O. Rodionov, "Enzyme-Inspired Functional Surfactant for Aerobic Oxidation of Activated Alcohols to Aldehydes in Water", *ACS Catalysis* **5**, 1313 (2015).

[2]J. Kestin, Khalifa, H. E., Correia, R. J., "Tables of the Dynamic and Kinematic Viscosity of Aqueous KCl Solutions in the Temperature Range 25-150 °C and the Pressure Range 0.1-35 MPa", *J. Phys. Chem. Ref. Data* **10**, 15 (1981).

[3]M. Venturi, Q.G. Mulazzani, and M.Z. Hoffman, "Radiolytically-Induced One-Electron Reduction of Methyl Viologen in Aqueous-Solution - Stability of the Radical Cation in Acidic and Highly Alkaline Media", *Radiation Physics and Chemistry* **23**, 229 (1984).

[4]E.S. Beh, D. De Porcellinis, R.L. Gracia, K.T. Xia, R.G. Gordon, and M.J. Aziz, "A Neutral pH Aqueous Organic-Organometallic Redox Flow Battery with Extremely High Capacity Retention", *ACS Energy Letters* **2**, 639 (2017).

[5]K. Lin, Chen, Q., Gerhardt, M. R., Tong, L., Kim, S. B., Eisenach, L., Valle, A. W., Hardee, D., Gordon, R. G., Aziz, M. J., Marshak, M. P., "Alkaline Quinone Flow Battery", *Science* **349**, 5 (2015).

385   [6]D.G. Kwabi, K. Lin, Y. Ji, E.F. Kerr, M.-A. Goulet, D. De Porcellinis, D.P. Tabor, D.A.
386   Pollack, A. Aspuru-Guzik, R.G. Gordon, and M.J. Aziz, "Alkaline Quinone Flow Battery with
387   Long Lifetime at pH 12", *Joule* **2**, 1907 (2018).
388   [7]M.A. Goulet and M.J. Aziz, "Flow Battery Molecular Reactant Stability Determined by
389   Symmetric Cell Cycling Methods", *Journal of The Electrochemical Society* **165**, A1466 (2018).
390   [8]Y. Ji, M.A. Goulet, D.A. Pollack, D.G. Kwabi, S. Jin, D. Porcellinis, E.F. Kerr, R.G. Gordon,
391   and M.J. Aziz, "A Phosphonate   Functionalized Quinone Redox Flow Battery at near   Neutral
392   pH with Record Capacity Retention Rate", *Advanced Energy Materials* **9**, 1900039 (2019).
393   [9]B. Hu, C. DeBruler, J. Moss, J. Luo, T. L. Liu, "A Sulfonate-Functionalized Viologen Enabling
394   Neutral Cation Exchange, Aqueous Organic Redox Flow Batteries toward Renewable Energy
395   Storage", *ACS Energy Letters* **3**, 663 (2018).
396   [10]T. Janoschka, N. Martin, M.D. Hager, and U.S. Schubert, "An Aqueous Redox-Flow Battery
397   with High Capacity and Power: The TEMPTA/MV System", *Angew Chem Int Ed Engl* **55**,
398   14427 (2016).
399